IOP Publishing Journal of Physics D: Applied Physics

J. Phys. D: Appl. Phys. **50** (2017) 093001 (28pp) doi:10.1088/1361-6463/aa53d7

Topical Review

Semi-transparent solar cells

J Sun[1,2] **and J J Jasieniak**[1,2]

[1] Department of Materials Science and Engineering, Monash University, Clayton, Victoria 3800, Australia
[2] Monash Energy Materials and Systems Institute (MEMSI), Monash University, Clayton, Victoria 3800, Australia

E-mail: Jacek.Jasieniak@monash.edu

Received 17 December 2015, revised 5 December 2016
Accepted for publication 14 December 2016
Published 3 February 2017

Abstract

Semi-transparent solar cells are a type of technology that combines the benefits of visible light transparency and light-to-electricity conversion. One of the biggest opportunities for such technologies is in their integration as windows and skylights within energy-sustainable buildings. Currently, such building integrated photovoltaics (BIPV) are dominated by crystalline silicon based modules; however, the opaque nature of silicon creates a unique opportunity for the adoption of emerging photovoltaic candidates that can be made truly semi-transparent. These include: amorphous silicon-, kesterite-, chalcopyrite-, CdTe-, dye-sensitized-, organic- and perovskite- based systems. For the most part, amorphous silicon has been the workhorse in the semi-transparent solar cell field owing to its established, low-temperature fabrication processes. Excitement around alternative classes, particularly perovskites and the inorganic candidates, has recently arisen because of the major efficiency gains exhibited by these technologies. Importantly, each of these presents unique opportunities and challenges within the context of BIPV. This topic review provides an overview into the broader benefits of semi-transparent solar cells as building-integrated features, as well as providing the current development status into all of the major types of semi-transparent solar cells technologies.

Keywords: semi-transparent, perovskite, solar cell, BIPV, bi-facial

(Some figures may appear in colour only in the online journal)

Abbreviation list

HVAC	Heating, venting and air-conditioning
BIPV	Building integrated photovoltaic
c-Si	Crystalline silicon
a-Si	Amorphous silicon
AM	Air mass
CIE	Commission Internationale de l'Éclairage International; International Commission on Illumination
TCE	Transparent conductive electrode
TCO	Transparent conductive oxide
ITO	Tin-doped indium oxide
FTO	Fluorine doped tin oxide
AZO	Aluminium doped zinc oxide
PEDOT:PSS	Poly-(3,4-ethylenedioxythiophene): poly(styrenesulfonate)
a-Si:H	Hydrogenated amorphous silicon
AVT	Average visible light transmittance
a-SiC:H	Amorphous silicon carbon alloys
Jsc	Short circuit current density
Voc	Open-circuit voltage
FF	Fill factor
PCE	Power conversion efficiency
CIS	CuInSe2
CGS	CuGaSe2
SLG	Soda-lime glass
CIGS	Cu(In,Ga)Se2
CZTS	Cu2ZnSnS2
CZTSSe	Cu2ZnSn(S,Se)2

CTO	Cd2SnO4
ZTO	ZnSnO*x*
DSSC	Dye-sensitized solar cell
PMMA	Poly-methyl-meta-acrylate
PANI	Polyaniline
PVP	Poly (vinyl pyrrolidone)
DMD	Dielectric–metal–dielectric
Spiro-OMeTED	(2,2′,7,7′-tetrakis-(N,N-di-p-methoxy-phenylamine)-9,9′- spirobifluorene)
CNT	Carbon nanotube
PSC	Perovskite solar cell
NW	Nanowire
HTL	Hole transport layer
CVD	Chemical vapour deposition
PDMS	Poly(dimethylsiloxane)
PC60/70BM	Phenyl-C61or71-butyric acid methyl ester
PET	Poly(ethylene terephthalate)
OPV	Organic photovoltaic
BHJ	Bulk-heterojunction
P3HT	Poly(3-hexylthiophene)
SQ	Shockley-Queisser
TT	Thieno[3,4-b]thiophene
BDT	Benzo[1,2-b:4,5-b′]dithiophene
PIDT-PhanQ	Poly(indacenodithiophene-co-phenanthro[9,10-b]quinoxaline)
PCPDTBT	Poly[2,6-(4,4-bis-(2-ethylhexyl)-4H-cyclopenta[2,1-b;3,4-b′]dithiophene)-alt-4,7-(2,1,3-benzothiadiazole)
PBDTTT-C-T	2,6-Bis(trimethyltin)-4,8-bis(5-(2-ethylhexyl)thiophen-2-yl)benzo[1,2-b:4,5-b′] dithiophene
DPP	Diketopyrrolopyrrole
BDTT	Thienylbenzodithiophene
ClAlPc	Chloroaluminum phthalocyanine
BCP	Bathocuproine
DBR	Distributed Bragg reflector
BBAR	Broad-band antireflection
Ph2-benz-bodipy	Benzannulated difluoro-bora-bis-(1-phenyl-indoyl)- azamethine
BPAPF	P-doped 9,9-bis[4-(N,N-bis-biphenyl-4-yl-amino) phenyl]-9H-fluorene
Alq_3	tris(8-hydroxy- quinolinato)-aluminum
PTCBI	3,4,9,10-perylenetetracarboxylic bis-benzimidazole
CuPc	Copper phthalocyanine
NIR	Near infrared
UV	Ultra violet
GZO	Gallium-doped zinc oxide

1. Introduction

The world is in the midst of an energy disruption. Underpinned by the Paris Agreement, a requirement to limit the atmospheric carbon dioxide levels to below 450 part per million compared to pre-industrial revolution times has been recognized as critical to ensure a sustainable environmental future for our planet [1]. A gamut of energy reduction measures and clean energy technologies will be required to achieve such a formidable goal. Of the possible energy reduction measures, integration of high efficiency lighting, low energy building design and optimized heating, venting and air-conditioning (HVAC) systems will continue to re-define building standards and policies around the world [2]. From an energy generation perspective, global energy trends are already showing drastic reductions in highly polluting, coal-based electricity generation [3], whilst photovoltaics and wind are exhibiting exponential growth [4]. For the world to meet its projected 28 TW energy demands by 2050 [5], energy generation technologies will have to be deployed at an equivalent rate of one standard power plant (~1 GW capacity) per day between now and then. This unprecedented level of energy generation deployment will necessitate continued renewable energy growth, as well as provide opportunities for new energy generation technologies to emerge.

Photovoltaics provided 242 GW of cumulative peak power globally in 2015 [6]. This represented an astounding 37% annual increase compared to 2014—the highest increase amongst all renewable technologies [7]. From a technological perspective, 93% of the entire photovoltaics market is currently dominated by crystalline silicon (*c*-Si) based modules [6]. Based on its established market presence and supply chains, it is highly likely that silicon will maintain its market leading role for rooftop and large scale solar installations [8]. Whilst beneficial from a sustainability perspective, this factor presents a fundamental development and adoption challenge for emerging photovoltaic technologies, unless clear disruptive cost or functional benefits can be demonstrated compared to existing silicon devices [9].

Semi-transparent solar cells that can be integrated into buildings as windows or skylights present this disruptive opportunity [10, 11]. These building elements play a fundamental role in mediating the energy use in modern buildings [12]. Not only do they provide the façade through which light enters a room, but, because they enable radiant heat to be transmitted and convective heat to be controlled, they are also one of the major heating/cooling elements [13]. Single and double glazed windows are standard for most commercial and emerging residential buildings for precisely this reason [10]. Developing energy efficient windows that can also harness electricity in a cost effective manner has been identified as a progressive next step towards energy efficient buildings (see figure 1 for examples).

The broader area in which solar cells are directly integrated into building elements, such as walls, roofs and windows, is termed building integrated photovoltaics (BIPV) [16]. At present, only 1% of the world's photovoltaic market is represented by BIPV [17]. Global policies around building energy use will contribute to major growth of this market; for instance, the European Directive 2010/31/EU has established that by 2020 all new building in the European Union will be required to be nearly energy neutral, i.e. 10 star rating [18]. To further add to this assessment, an analysis of the BIPV markets has indicated that the low cost of rooftops and their limited space compared to building facades/windows, will

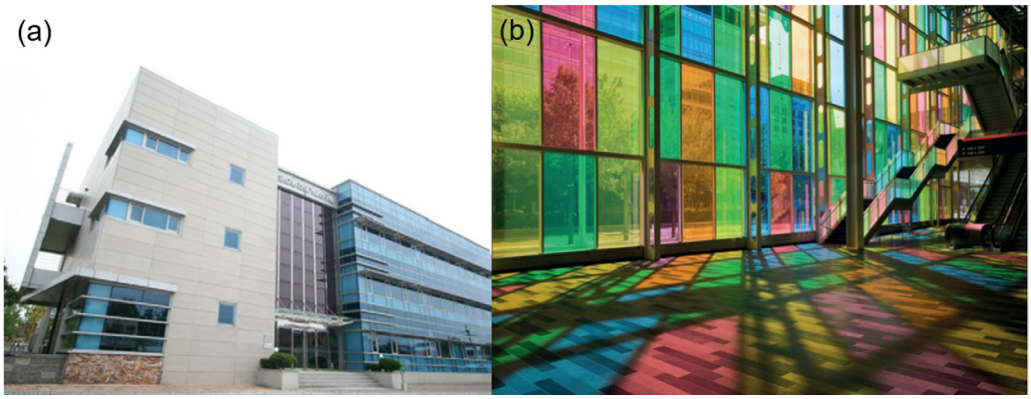

Figure 1. (a) Transparent thin-film BIPV modules on the Kolon E&C R&D Institute (Korea). Adapted with permission from [14]. © 2011, Elsevier. (b) The striking BIPV façade of the Palais des Congrès in Montreal. Reprinted with permission from [15]. © 2015, Nature.

ensure that energy generating facades/windows will provide the strongest value proposition for successful market penetration in the future [19]. These factors alone will contribute to the market value of BIPV glass products increasing from $800 million in 2014 up to $2.7 billion by 2019 [20].

The above assessments highlight the imminent opportunity for deployment of semi-transparent solar cells within building products. For this to occur, technologies are required that are low-cost, efficient, have long-term stability and possess the appropriate architectural aesthetic characteristics [21]. For opaque building elements, such as walls, *c*-Si photovoltaics has emerged as a technological champion owing to reasons given above [22, 23]. For semi-transparent building elements, the majority of existing BIPV have also historically been *c*-Si or amorphous silicon (*a*-Si) devices [24]. It is important to note that of these, *c*-Si based technologies should strictly speaking be considered 'semi-opaque', as they are fabricated from opaque *c*-Si devices that are tiled within a transparent laminate to provide a specific transparency (see figure 2(a)). In contrast, *a*-Si devices can be more correctly termed 'semi-transparent', but only if they enable light to be transmitted through the active photovoltaic materials (see figure 2(b)). This property is common to solar cell technologies that: (i) can be fabricated on transparent substrates; (ii) have transparent electrodes; and (iii) can be molecularly and/or structurally engineered to permit sufficient visible light transmission.

Over the past three decades, a host of inorganic [25], organic [26–28], dye-sensitized [29] and more recently, hybrid perovskite [30] photovoltaic technologies have emerged that can be integrated into semi-transparent solar cells devices. Although each of these technologies possesses various benefits and drawbacks, major efficiency gains across inorganic and perovskites has pushed device solar-to-electricity efficiencies close to the best *c*-Si photovoltaics [31]. This places semi-transparent solar cells at an important cross-road that will likely mark a transition to non-silicon based technologies for window applications.

The purpose of this article is to review the technological evolutions that have been taking places across the relevant semi-transparent solar cells and to provide comparative insights into each technology to date. For brevity, we limit the discussions around semi-opaque devices in this review as these

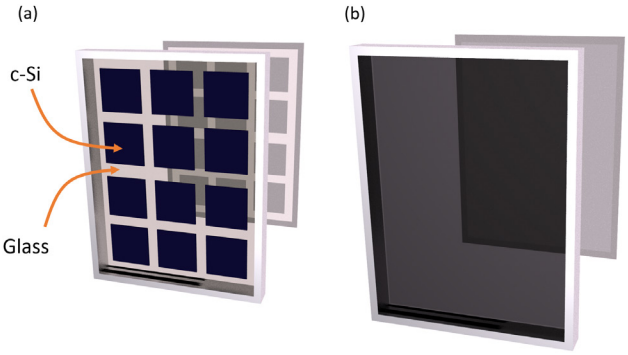

Figure 2. A schematic depiction of (a) semi-opaque and (b) semi-transparent solar cell device architectures.

are well developed at this point [24, 32]. Having provided the environmental and commercial impetus for semi-transparent photovoltaic devices already, we have organized the remainder of this review according to the following three sections:

(i) BIPV requirements and benefits: The spectral characteristics of photovoltaics integrated into buildings as windows, facades or blinds different from that of standard roof-top solar. This section provides a fundamental basis from which to understand these variations, the requirements of semi-transparent photovoltaic devices and the practical limitations of such devices.

(ii) Semi-transparent photovoltaic technologies: An overview into the various technologies available for semi-transparent solar cell applications. This includes a description into the working principles of the different technologies, their benefits and drawbacks.

(iii) Challenges and future opportunities: Discussion on some of the major challenges that still exist across the reviewed semi-transparent technologies and opportunities in going forward.

2. BIPV requirements and benefits

The spectral characteristics of solar irradiation incident on the Earth's surface is highly dependent on the geographic location, the season, the weather and the exact time of day. For

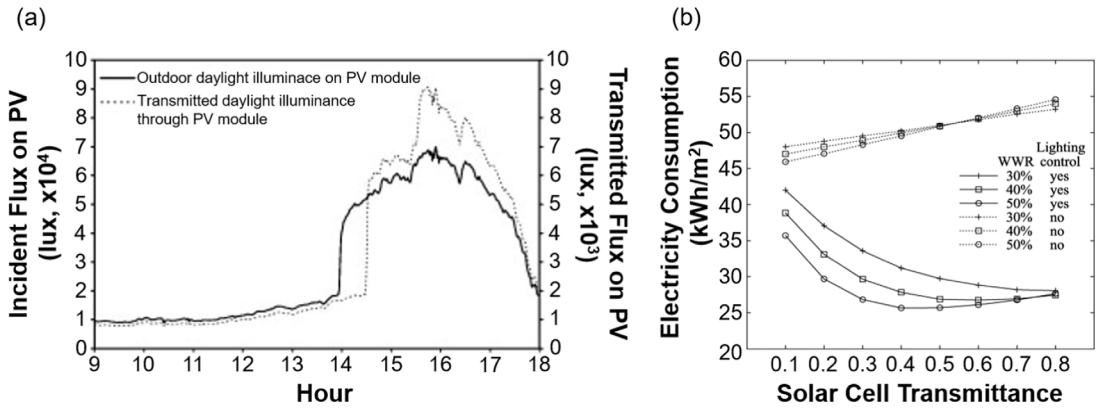

Figure 3. (a) Measured outdoor irradiance of a west-facing window within an office building in Hong Kong. The indoor irradiance shown is that following transmittance through a 10% average visible transmittance semi-transparent photovoltaic module integrated with the window. Adapted with permission from [37]. © 2009, Elsevier. (b) The relative electricity consumption of an office building with integrated semi-transparent photovoltaic windows of varying visible transmittance with and without lighting control. Reprinted with permission from [12]. © 2005, Elsevier.

standard solar cell testing, the air mass (AM) 1.5 standard has been universally adopted and is defined as sunlight directly incident at a zenith angle of 48.2° with an intensity of 1000 W m^{-2} across the entire spectral range [33]. Evidently, light that is incident onto building facades occurs under non-standard conditions, stemming predominantly from the visible sky, with both direct and diffuse contributions present, and from reflection below the horizon, e.g. buildings. To tackle this, and related weather variations, the International Commission on Illumination (CIE) has established a set of 15 standard conditions that define relative sky luminance values across a broad range of clear, intermediate and overcast conditions that may be presented globally [34]. It is not within the scope of the current review to outline these standards; however, we note that these can be used for simulating different solar illumination conditions present on a building through, for instance, a Waldram diagram formalism with a 3D environmental map [35, 36]. Practically speaking, studies of the illumination on real building facades on clear days have shown that solar intensities below 600 W m^{-2} are typical under direct illumination and $<$100 W m^{-2} under diffuse conditions [37, 38]. Based on the CIE standards, clouds and pollution are predicted to reduce the magnitude of the direct component and modify the relative breakdown between both contributions.

As is shown in figure 3(a), for an exemplary case of a west facing window in Hong Kong, the diffuse and direct solar irradiance contributions change during the course of a normal sunny day [37, 39]. In this case, the direct sun enters the building only in the afternoon, whilst at other times only the diffuse contribution is present. This indicates that the illumination conditions for BIPV on horizontal facades are lower and more diffuse compared to traditional rooftop solar. As a result, BIPV products require solar cells that possess high efficiencies at relatively low illuminations and under highly diffuse conditions.

From a building perspective, the diffuse and direct contributions incident on a building's windows provide complexity in managing the lighting and heating/cooling requirements. Firstly, when the transmitted solar intensity is in excess of ~95 W m^{-2}, glare becomes problematic for workings within buildings [40]. Meanwhile, at sufficiently low levels, artificial lighting is required to ensure lighting level standards are met—these typically range between 3 and 30 W m^{-2} depending on the specific building location [41]. Secondly, in cooling dominated climates, such as Australia, Hong Kong and California, the peak electricity demand occurs concurrently with that of the cooling load demand. As solar light provides a radiant source of heating, additional cooling requirements are necessary during times of direct illumination.

Glazed windows with an average transmittance across the visible region of between 10 and 60% overcome these challenges by balancing the natural light admission into a building, while maintaining the reduced cooling and lighting demands [42]. Semi-transparent solar cells provide these benefits and the additional feature of electricity generation [16, 43]. Case studies of semi-transparent solar cell integration within buildings have shown clear benefits in terms of electricity savings and reduction of peak loads within office and residential buildings. Li *et al* has for instance suggested that semi-transparent solar cells installed on one side of a high-rise office building coupled with light dimming can readily enable electricity savings of up to 12% compared to single glazed windows [37]. Miyazaki *et al* have shown that full integration of semi-transparent photovoltaic windows within a multi-zoned building design that also has light dimming can result in energy reductions of up to 55% compared standard single glazed windows [12]. In that work, the authors demonstrated the necessity of coupling the semi-transparent photovoltaic facades to internal light control to reduce electricity consumption whilst enabling a higher solar transmittance to be maintained (see figure 3(b)). Under optimal conditions, the transparency across the visible for the windows was 40%, which provides a practical gauge for future technologies. Beyond office buildings, semi-transparent solar cells have also been deployed within roofing structures, for which energy consumption has also been reduced by up to 8% compared to roofs with integrated opaque photovoltaic modules [10].

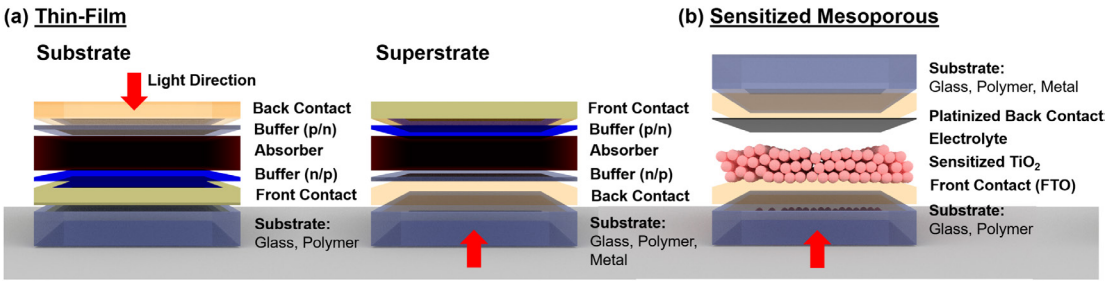

Figure 4. Schematic of the three representative device structures that have promise for use within semi-transparent solar cells. These can be largely separated into two major classes: (a) thin-film and (b) sensitized mesoporous.

Each of these examples highlight the lucrative case for the integration of semi-transparent solar cell devices into buildings. Moreover, they also show that for such devices to have maximum impact on building efficiency, they have to be considered in conjunction with light optimisation approaches. Both of these factors have to be optimised based on the geographic location of the building, the surrounding urban design and specific direction of the window. Overarching all of these is the need to have the highest solar cell device efficiencies possible. The following section outlines the various semi-transparent solar cell technologies that are currently being developed to potentially power our future buildings.

3. Semi-transparent photovoltaic technologies

In this section we will highlight the advances across the major solar cell classes that have emerged with potential promise for semi-transparent applications. These can be largely separated into inorganic (e.g. CdTe, Cu_2ZnSnS_4 or $CuInSe_2$), organic (e.g. poly(3-hexylthiophene): Phenyl-C_{61}-butyric acid methyl ester bulk heterojunctions (BHJ)) or perovskite (e.g. methalyammonium lead iodide) thin film or meso-porous (e.g. dye or quantum dots) sensitized solar cell architectures.

Thin films devices harness materials with absorption coefficients greater than 10^4 cm^{-1} that are sandwiched between charge selective electrodes, typically within 'superstrate' or 'substrate' device configurations (figure 4(a)). The high absorption coefficients enable the majority of visible light to be absorbed in a thickness range of 0.1–5 μm. In the 'superstrate' configuration, light enters through a transparent substrate, passes through a transparent conductive electrode (TCE) and any charge selective layers, then is absorbed within the active layer. A modified back contact is deposited onto the active layer to provide charge selective transport and a collecting electrode. For opaque devices the electrode at this back contact is typically metal, whilst for semi-transparent devices it is a TCE. In the 'substrate' configuration, light is incident from the opposing side onto the front TCE. By nature, this necessitates that the back contact is deposited onto the substrate. One of the major advantages of 'substrate' configurations are that opaque substrates can be used, which is clearly not suitable for semi-transparent solar cell architectures.

Sensitized solar cells on the other hand are most commonly fabricated using a mesoporous layer of semi-conducting nanoparticulates (e.g. TiO_2), which are sintered on a TCE electrode that is hosted on a transparent substrate [44]. Sensitizers are adsorbed onto the mesoporous scaffold films to provide type-II interfaces that can induce charge separation and drive the photocurrent. The devices are complete through the use of a solid or liquid electrolyte and a counter electrode (cathode), which is typically made by platinum (Pt) catalyst coated fluorine doped tin oxide (FTO) glass (figure 4(b)).

For fabricating high power-conversion-efficiency (PCE) semi-transparent solar cells, the conductivity, transparency and structure of the TCEs have to be considered. Technically speaking, existing smart windows already deploy TCEs within their device architecture [45]. In such technologies, metallic and metal oxide coatings are introduced onto glass to control the amount of visible and infrared light that is reflected and transmitted [46]. Metallic window coatings for such applications typically constitute very thin layers of metal (5–50 nm) that are either directly deposited on glass or introduced through a polymer-based laminate onto one of the glass surfaces [47]. Such coatings harness additional inert metal oxide layers to enhance their mechanical and optical properties [48]. Meanwhile, the transparent conductive oxide (TCO) coatings are fabricated from degenerately doped and high optical bandgap oxides, such as *n*-type tin-doped indium oxide (ITO), aluminium doped zinc oxide (AZO) and FTO [45, 49]. Advantageously, both metal and oxide coatings can be made semi-transparent and possess sheet resistances values as low as 5 Ω sq^{-1}, which makes them ideal as potential electrodes for semi-transparent devices. The ability to harness these existing electrodes within smart windows presents one of the biggest opportunities for developing semi-transparent solar cells.

On the counter electrode side, TCEs with sufficient conductivity have been achieved through a variety of approaches, including nanowires (e.g. Ag, Cu, Au) [50], polymers (e.g. poly-(3,4-ethylenedioxythiophene): poly(styrenesulfonate) (PEDOT:PSS)) [51], electrochemically deposited layers (e.g. Pt) [52], thermally deposited layers (e.g. Al, Ag, Au) [53] and sputtered layers (e.g. ITO, FTO, AZO) [54]. Each of these present their own merits for particular device structures and fabrication processes. As we proceed in this review, these will now be addressed in the context of the different semi-transparent solar cell device architectures.

3.1. Amorphous silicon (a-Si)

Hydrogenated amorphous silicon (*a*-Si:H) was first discovered by Chittick *et al* in 1969 [55]. Its high, direct bandgap ($E_{g,direct}$ ~ 1.7 eV) and 10-fold larger absorption coefficients

across the visible region compared to *c*-Si ($E_{g,indirect}$ ~ 1.1 eV), spawned tremendous activity in its use for a variety of opto-electronic applications, including solar cells, which by the 1980's exhibited efficiencies of ~10% [56]. These devices were fabricated in both 'superstrate' and 'substrate' configurations with *p–i–n* architectures between the electrodes. In this structure light absorption takes places in the intrinsic '*i*' region and the *p*-type (*n*-type) doped silicon layers provide the high (low) work function to create an electric field across the device and form charge selective contacts [57]. Typical TCO's such as FTO or doped ZnO (e.g. ZnO:Al) have been used as electrodes and optical spacers. Despite the significant early progress for such devices, it was quickly realized that *a*-Si:H was unstable under light exposure through the so-called Staebler–Wronski effect [58]. This has effectively limited the stabilized efficiencies of such devices to a record PCE of 10.2%, with short-circuit current (J_{sc}) = 16.36 mA cm^{-2}, open-circuit voltage (V_{oc}) = 0.896 V and fill-factor (FF) of 0.698 [31].

The low-temperature processing and flexibility in device structure of *a*-Si:H has provided significant commercial interest for BIPV applications [24, 59, 60]. Early advances in these technologies showed that by employing TCO's as bottom and top electrodes (particularly doped ZnO and SnO_2 varieties), semi-transparency could be achieved by structuring microholes within the *a*-Si:H absorber layers or thinning the absorber layers to <100 nm [61–64]. These semi-transparent *a*-Si:H devices possessed efficiencies of ~6% with 25% average visible transmission (AVT) in the late 1980's. Major research efforts by the likes of Sanyo, Shott and others resulted in significant developments in scaling of such devices to create numerous semi-transparent commercial products in the 2000's. Few of these are left, with manufacturers that remain providing solar cells with claimed PCEs that range between 4 and 6% at 5–20% AVTs (e.g. Sun Well Solar and Kaneka) [39]. As a comparison, on a lab scale, the best devices provide PCEs that approach 6–7% with a visible transmission of ~20–25% [65].

Research in this area still continues, particularly around bandgap tunability. A recent report looked at the fabrication of semi-transparent devices with the introduction of germanium to form amorphous silicon germanium (*a*-$Si_{0.8}Ge_{0.2}$:H) [66]. As is well known, the introduction of Ge provides an easy ability to reduce the bandgap in these cells at the cost of V_{oc} [67]. Such devices were grown in a conventional manner from silane (SiH_4) and germane (GeH_4) within a partially hydrogenated environment at 250 °C on a gallium doped ZnO (ZnO:Ga) TCO. The cells were fabricated in a conventional *p–i–n* structure, where ZnO:Ga also served as the top electrode. These devices were grown with an active layer thickness of 150 nm to ensure transparency and possessed a PCE of 5.9% at an AVT of 17.9%. The comparison device with no Ge possessed a PCE of 5.5% at a high visible transparency of 21.6%. This suggests that for a comparable thickness there is a compromise in transmittance to achieve the marginal increase in efficiency in this system.

Amorphous silicon carbon alloys (*a*-SiC:H) have also been used in semi-transparent devices. Such materials possess increasing optical bandgap at higher carbon content, at the cost of reduced photoconductivity [68]. Using an alloy with an optical bandgap of 2.19 eV, Gao *et al* made *p–i–n* 'superstrate' devices on Glass/FTO with an active layer thickness of only 60 nm [69, 70]. The PCE was only 1%, with transparencies of >30% being noted across the visible. The study showed a functional limit of 40 nm for the minimum absorber thickness due to the formation of pin-holes and V_{oc} losses arising from enhanced surface recombination. Whilst the efficiency was low, the device characteristics were sufficient to operate an electrochromic device integrated in tandem. In a modified approached, Henaki *et al* harnessed a microcrystalline layer within a (μc-Si)-*p*(*a*-SiC:H)-*i*(*a*-SiC:H)-*n*(μc-Si:H) heterojunction to demonstrate device PCEs of up to 6.3% [71]. Although modest, this value is on par with conventional *a*-SiC:H and, thus, presents limited advantages for BIPV applications.

Ultimately, the major limitations of *a*-SiC:H device remain around device stability and low device efficiencies. Whilst significant efforts have been expanded to overcoming these, there is no clear pathway forward. As a mature technology, this naturally indicates that more opportunity exists in alternate material systems for future BIPV applications.

3.2. I–III–VI$_2$ Chalcopyrites

The exploration of I–III–VI_2 chalcopyrites within photovoltaics began in the 1970s with $CuInSe_2$ (CIS) as the material of choice [72]. The field evolved in the 1990's when Ga started to be alloyed into the structure as a means to tune the optical bandgap from 1.0 eV (CIS) to 1.7 eV ($CuGaSe_2$ (CGS)) [73]. With progressive device engineering, efficiencies rapidly improved to levels that approached 19% in the late 90s [74]. These levels were saturated until Tiwari's group recently advanced the field through the use of potassium fluoride to passivate surface defects and reduce optical losses to achieve device efficiencies above 20% [75]. The record PCE is currently at 22.3%, with J_{sc} = 39.38 mA cm^{-2}, V_{oc} = 0.422 V and FF of 0.782 [31].

All high-efficiency Cu(In,Ga)Se_2 (CIGS) devices are fabricated in a 'substrate' configuration that consists of TCO/buffer/CIGS/back-electrode/soda-lime glass (SLG) [76]. For opaque devices, numerous combinations of these have been trialed, with the best-to-date front-contact being provided by AZO/intrinsic ZnO (*i*-ZnO)/*n*-type CdS and the back-electrode being molybdenum. The most successful approaches for fabricating the CIGS layer have been through a three-stage co-evaporation process of the individual elements at temperatures above 550 °C [73]. All additional layers on the CIGS are deposited at 200 °C or below to enable the interfaces to be highly optimized in terms of strain and inter-diffusion.

A number of authors have investigated replacing the molybdenum electrode to successfully fabricate 'semi-transparent' CIGS on SLG (figure 5(a)) [77–79]. As is shown in figure 5(b), Nakada *et al* assessed the performance of the

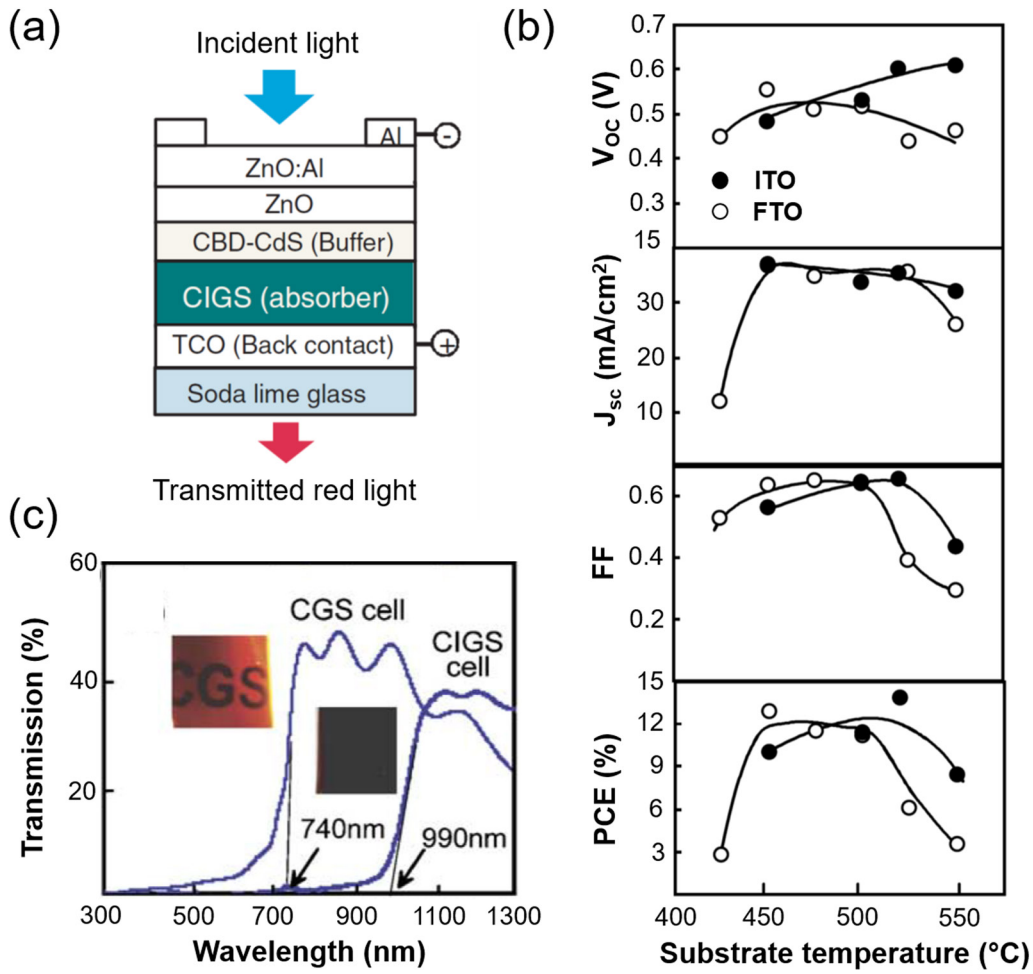

Figure 5. (a) Substrate device structure used with a transparent conductive oxide back contact. (b) The solar cell device parameters for CIGS devices fabricated at various deposition temperatures of the CIGS on ITO and FTO back contacts. (c) The transmittance spectra of CIGS and the equivalent $CuGaSe_2$ solar cells, with the optical micrographs of the devices as insets. Reprinted with permission from [78]. © 2004, Elsevier.

devices fabricated with the FTO, ITO or ZnO:Al transparent electrodes as a function of the CIGS deposition temperature [78]. Devices fabricated using ITO were optimized at 520 °C and showed an efficiency of 15.2%. The authors suggested that in the case of ITO, the limiting thermal stability stemmed from segregation of n-Ga_2O_3 between the ITO and CIGS layers, which acted to reduce the built-in electric field in the device. Notably, it is well known that ITO exhibits thermal instability; however, this is only under oxidising environments [80]. Under the vacuum deposition conditions used for the co-evaporation of the CIGS layers, the ITO was stable up to the segregation temperature. In comparison, the devices using an FTO electrodes showed optimized devices at a lower deposition temperature of 500 °C, with an efficiency of 13.7%. It was suggested that higher annealing temperatures resulted in the loss of fluoride from the FTO. Finally, experiments conducted using AZO showed devices with almost zero efficiency. The n-Ga_2O_3 segregation was also considered as the possible reason for this; however, an equally likely explanation lies in the significantly lower work function of this electrode in comparison to both ITO and FTO [81], which creates negligible electric field across the device for charge extraction. It should be noted that the recent developments around processing of CIGS, which have enabled efficiencies approaching 20% to be achieved at temperatures of 500 °C and below, could readily be applied to the above device architectures and increase the noted efficiencies considerably [82].

Complimentary studies on using evaporated CGS on ITO instead of CIGS have also been carried out [83]. These have yielded single-junction devices with PCEs $<5\%$. The opportunity for CGS lies in its use within tandem structures in conjunction with CIGS [79]. As such, whilst these single-junction efficiencies are low, there is an opportunity to potentially harness such devices in stacked or bifacial tandems for BIPV applications.

One of the caveats of the above works is that their claim to 'semi-transparency' is not consistent with the requirement for BIPV. In these devices the CIGS layers were >2 microns thick, which rendered them partially transparent in the infrared region, but not in the visible (figure 5). To successfully develop visibly semi-transparent devices, the thickness of the CIGS layer has to be reduced to sub-micron levels. Numerous studies have shown that at these thicknesses, CIGS devices suffer from reduced V_{oc}, J_{sc}, FF and enhanced shunting [84–86]. These problems have to be resolved to fully exploit the above devices architectures as truly semi-transparent applications.

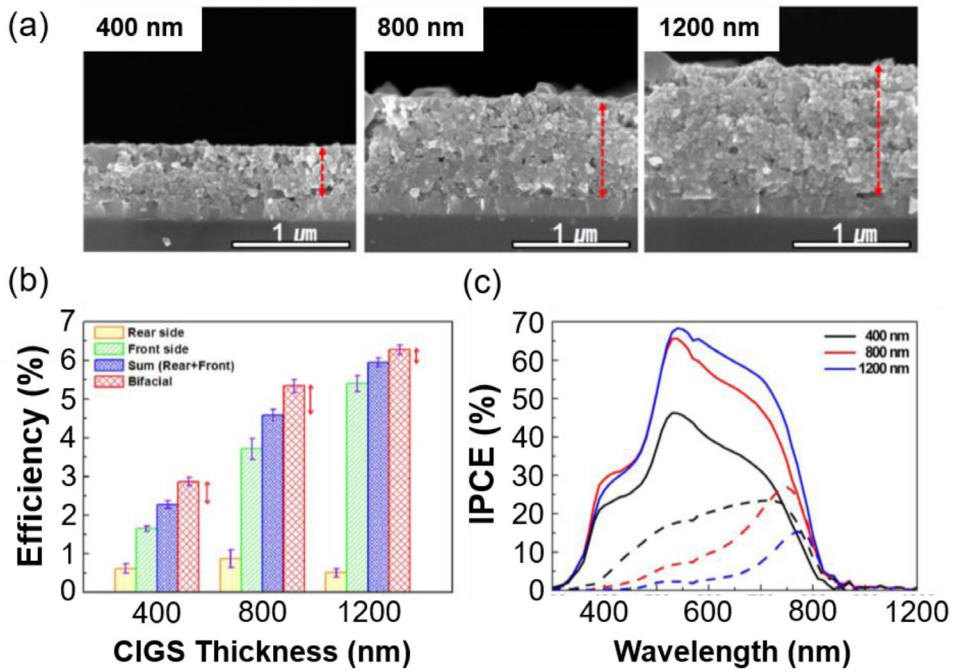

Figure 6. (a) Scanning electron micrographs of CIGS layers deposited from molecular precursor solutions. (b) Device efficiencies of the CIGS devices illuminated under different conditions. (c) Incident-to-photon-conversion (IPCE) efficiencies for front (solid lines) and back (dashed lines) illuminations. Reprinted with permission from [91]. © 2014, Nature.

Progress in this direction was recently demonstrated by Saifullah *et al*, who investigated the role of silver gallium sulphide interlayers between the ITO and CIGS layer [87]. The authors showed that the inclusion of this layer enabled the V_{oc} to be maintained at ~0.7 V, even for CIGS thicknesses as low as 230 nm. Through these advances the authors demonstrated truly semi-transparent device structures with a record PCE of 5.9% at an AVT of 25.5%. This represents the most efficient semi-transparent CIGS device in the literature.

All the above studies have used vacuum-based techniques for depositing the CIGS layers. There is an opportunity to exploit solution-processing as an alternative route to render scalable and low-cost production, provided that comparable efficiencies can be demonstrated [88]. Nanoparticle and hydrazine approaches for opaque device architectures have been the most successful to date, yielding device efficiencies of >15% [88, 89]. However, very little effort has been made to translate these advances to semi-transparent device architectures with the same efficiency [90, 91]. In figure 6 we highlight the work of Moon *et al*, who used molecular precursors for developing semi-transparent devices on ITO [91]. The authors fabricated nanocrystalline CIGS layers with thicknesses down to 400 nm (figure 6(a)), which rendered them suitable for semi-transparent applications. As can be seen in figure 6(b), the progressive increase in CIGS thickness from 400 nm to 1200 nm resulted in a concomitant increase in device efficiency, with that from front illumination rising from 1.7% to 5.6%. As touched upon above, this trend predominantly arises from reduced V_{oc}, FF and J_{sc}, owing to the reduced incident conversion efficiency, at the lower thicknesses (figure 6(c)).

To date, the efficiencies of semi-transparent CIGS films have remained low in comparison to their opaque analogues. With the recent developments around low-temperature processing and the emergence of novel TCEs, it is envisaged that this area will exhibit continued improvement, particularly owing to the inherent photo and chemical stability of CIGS.

3.3. *I–II–IV–VI$_4$ kesterites*

As a structural cousin of chalcopyrites, kesterite Cu_2ZnSnS_2 (CZTS) and $Cu_2ZnSn(S,Se)_2$ (CZTSSe) have recently emerged as suitable alternatives to CIGS absorbers owing to their low cost, earth-abundance and equally promising optoelectronic properties [92]. These materials were first discovered in 1966 [93], with their photovoltaic qualities being recognized in 1988 by Ito and Nagazawa [94]. The development of kesterite devices has leveraged significantly from progress in CIGS, with identical 'substrate' device architectures being adopted. To date, both vacuum and solution-processed approaches have been pursued concurrently, with particular successes for the latter stemming from hydrazine [95], molecular precursor [96] and nanoparticle approaches [97, 98]. The record PCE for opaque CZTS devices is currently 9.1%, with a $J_{sc} = 20.84$ mA cm^{-2}, $V_{oc} = 0.701$ V and FF of 0.625, and for CZTSSe it is 12.6%, with a $J_{sc} = 35.21$ mA cm^{-2}, $V_{oc} = 0.513$ V and FF of 0.698 [31].

The major challenge for these materials lies in the processing of the main absorber to ensure that the bulk and surface defects are minimized, which currently limit the V_{oc} and FFs compared to equivalent CIGS devices [94]. Whilst a significant research effort is currently under way to solve these issues, the technology is still in its formative stage, which has meant that very little attention has been given to semi-transparent kesterite devices. Drawing inspiration from the work on bi-facial CIGS solar cells reported by Nakada [77],

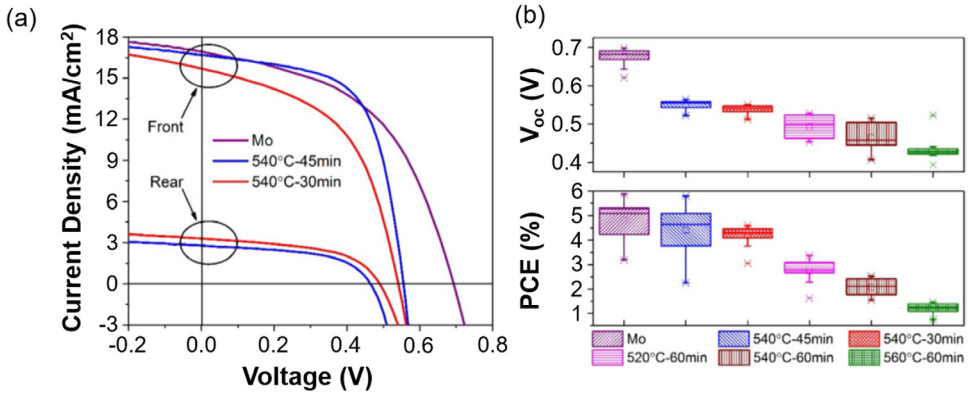

Figure 7. (a) Current-voltage and (b) device characteristics of CZTS devices fabricated on ITO and Mo back electrodes in a substrate configuration processed under different annealing conditions. Reprinted with permission from [103]. © 2016, Wiley-VCH Verlag GmbH and Co. KGaA.

early works by Sarswat *et al* in 2011–12 showed that CZTS layers could be grown on FTO using sol-gel [99] or electrochemical [100] methods at temperatures between 475 and 550 °C. Adopting the electrochemical approach, Ge and workers were the first to report on using kesterites in bifacial solar cells in 2014 [101]. The authors investigated the behaviour of CZTS grown on ITO electrodes using H_2S as a sulfurizing agent at 520 °C. Fabricated devices showed a front-illumination efficiency of 2.9%. Despite these modest efficiencies, the study clearly showed that annealing under H_2S adversely impacted the ITO conductivity and encouraged the interfacial reaction between the CZTS, which created a non-ohmic back contact.

Replacing the highly reactive H_2S with the more benign elemental selenium [102] or sulphur [103] during the high temperature processing step, enabled the formation of CZTSSe and CZTS devices with significantly reduced ITO instability, even at temperatures of 550 °C. The CZTSSe devices were limited in efficiency to ~1.8%; however, the CZTS devices showed a drastic improvement to 5.8%. In both cases the diffusion of indium into the CZTSSe layers was observed, which at higher temperatures and longer processing times detrimentally resulted in significant SnO_2 formation at the ITO contact. Notably, indium incorporation into CZTS has been shown to increase the carrier density, enhance mobility and improve V_{oc} due to the formation of shallow In_{Sn} defects [104, 105]; however, as seen in figure 7, the above CZTS devices exhibited a significant V_{oc} deficit compared to equivalent devices deposited on Mo. At this stage it is not clear whether this deficit arises from the residual SnO_2 at the back interface or the uncontrolled indium diffusion.

Solving such interfacial research question is vital to progress this technology to levels that parallel the developments of their opaque analogue devices. Whilst the infrared semi-transparent devices discussed above lend themselves to being visibly semi-transparent, all have been fabricated with kesterite layers of thickness greater than 500 nm, for which visible transparency is limited. As such, to the best of our knowledge, at present there have been no reports of visibly semi-transparent kesterite solar cells.

3.4. CdTe

CdTe is the most commercially successful thin film absorber used in solar cell technologies in the world. The electronic properties of this material were discovered in 1947 [106], but it wasn't until 1956 when it was reported as a potential photovoltaics candidate [107]. Since that time, it has progressed from single-crystal based solar cells through to thin-film architectures, largely owing to its large absorption coefficient ($>10^4$ cm^{-1} across the entire visible), ease of processing, high stability and nearly ideal optical bandgap for single-junction solar cells [108, 109]. One of the major challenges in CdTe has historically been achieving ohmic contact at the cathode layer. As a result, 'substrate' device structures have been typically hindered by contact barriers limitations [110]. For this reason, all high efficiency CdTe devices have been fabricated using 'superstrate' configurations, in which greater control of the cathode is rendered. For typical 'substrate' CdTe devices, the TCO, conventionally FTO, is coated with an intrinsic blocking layer, e.g. *i*-SnO_2, and almost university an *n*-type CdS hole blocking layer. Onto this stack, the CdTe is most commonly deposited using close space sublimation, although a host of other approaches have been investigated [108, 111]. The back contact at the cathode is engineered through a thin buffer layer of metal that can react at the interface (Cu, Ni, Sb, etc) and/or a metal-chalcogenide layer (ZnTe, $CuTe_x$, Sb_2Te_3, etc) and then finished with metal electrode (Au, Mo, Al, etc) [112]. Leading progress in this area has been made by First Solar, who have fabricated devices with record PCEs of 22.1%, $J_{sc} = 31.69$ mA cm^{-2}, $V_{oc} = 0.887$ V and FF of 0.785 [31].

By nature of the 'superstrate' configuration, the development of semi-transparent solar cells requires two key elements: (i) the use of a transparent top electrode and (ii) the thinning of the CdTe to thicknesses of less than 400 nm. The earliest work towards such devices was reported in the late 1980's by Birkmire *et al*, who used ITO as the top electrode with a 2 nm copper interlayer on the CdTe to facilitate interfacial and bulk doping [113]. The devices consisted of 2 micron thick CdTe and were only semi-transparent in the sub-gap region of CdTe

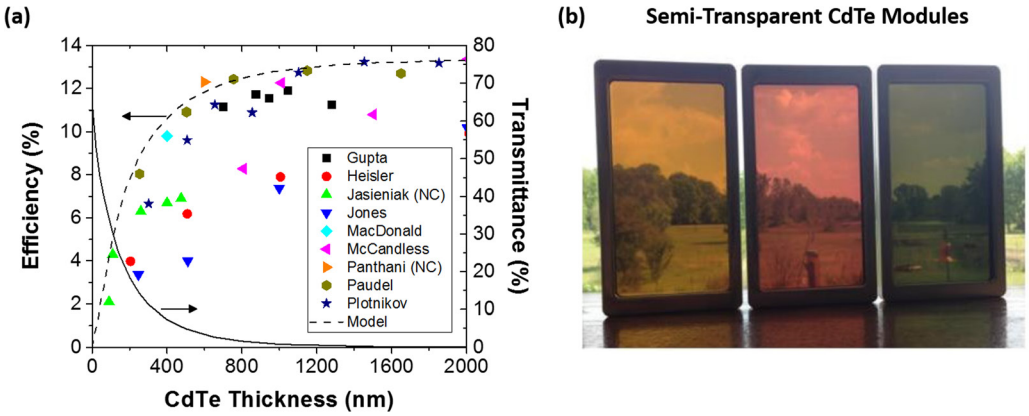

Figure 8. (a) Efficiency of selected opaque CdTe solar cell devices at different CdTe thicknesses from the following references: Gupta [128]; Heisler [126]; Jasieniak [123]; Jones [129]; MacDonald [130]; McCandless [131]; Panthani [132]; Paudel [122]; Plotnikov [133]. The inclusion of NC within the legend indicates that these devices were fabricated using nanocrystal inks, whilst all other devices used vacuum-based processing. Included is a model of the thickness-dependent efficiencies of such devices from [122], which considers the thickness-dependent voltage and current limitations. As a comparison, the calculated transmittance as a function of CdTe thickness within a semi-transparent Glass/ITO (150 nm)/*i*-ZnO (50 nm)/CdS (80 nm)/CdTe/ITO (150 nm) solar cell architecture is presented. (b) Semi-transparent CdTe mini-modules with selective light absorbers for colour modification. Reprinted with permission from [127]. © 2013, IEEE.

(<1.5 eV). Optimized devices exhibited an efficiency of 8.4%. Similar device structures were investigated decades later by Tiwari, who achieved comparable device performances and showed the importance of minimising the copper thickness to ensure device stability [114, 115]. Progress in this device structure continued through the inclusion of a ZnTe:Cu electron blocking layer between the CdTe and ITO electrode, thereby boosting efficiencies up to ~10% [116–118]. The greatest developments in this space stemmed from substitution of the ZnTe by Cu_xTe and replacement of the FTO electrode by the more transparent cadmium stannate (Cd_2SnO_4, CTO), which was coated with a zinc stannate ($ZnSnO_x$, ZTO) buffer and a nanocrystalline CdS:O hole blocking layer [119]. These devices possessed an infrared transmission of ~50% and a certified PCE of 13.9%.

Whilst all of the above devices can enable semi-transparency, they were designed with thick CdTe layers of >2 μm to function within tandem solar cells or as bi-facial devices. For visibly semi-transparent devices thinning of the absorber layer is required, which, much like for CIGS devices, presents major challenges for CdTe due to shunting and V_{oc}, J_{sc} and FF losses [109, 120, 121]. These challenges are depicted in figures 8, where the practical efficiency limits of opaque devices with varying CdTe thickness are shown and compared to that based on a simple model derived in [122]. It is important to note, that the best ultra-thin CdTe devices have been fabricated from solution-processed nanocrystal inks, which are denoted as NC within figure 8(a) [123].

To gauge how these trends will impact visibly semi-transparent solar cells, we have simulated the AVT across the 400–800 nm spectral range of a glass/ITO (150 nm)/*i*-ZnO (50 nm)/CdS (80 nm)/CdTe/ITO (150 nm)/Air semi-transparent device for various CdTe thicknesses using the transfer matrix approach (see figure 8(a)) [124]. These transmittance values include all the parasitic contributions arising from the device structure itself. Evidently, to achieve an AVT of ~10%, the minimum one would consider implementing within BIPV windows, the CdTe layer has to be less than ~400 nm in thickness. At this thickness, PCE would be much less than 11%, which is the practical limit for opaque devices.

This thickness regime is a challenge for CdTe devices to be fabricated with high efficiency. The group of Compaan has made CdTe devices with a 680 nm thick CdTe active layers and a ZnTe:N/ITO transparent back electrode, with champion devices possessing efficiencies of >5% for front and back electrode illumination [125]. As expected, comparable device characteristics were achieved using a Cu–Al/ZnO:Al electrode for a similar CdTe thickness [126]. Whilst examples of semi-transparent CdTe solar cells below these thickness values have been presented (see figure 8(b)), we could not find any reliable device characteristics [127]. This may arise from commercial sensitivities by companies such as Lucintech, but likely also reflects the challenges presented in achieving high efficiencies due to the drastic reduction in V_{oc} at the required thicknesses to achieve semi-transparency.

3.5. Dye-sensitized solar cells

Dye-sensitized solar cells (DSSCs) were first demonstrated by O'Regan and Grätzel in 1991, when they sensitized a mesoporous TiO_2 nanoparticles electrode with a monolayer of ruthenium dye to recognize a step-change improvement in the photocurrents and, thus, efficiencies compared to planar devices [29]. The original devices possessed an efficiency of up 8% under normal light conditions and 12% under diffuse conditions, with the enhanced efficiency under low-light conditions being recognized early as a lucrative feature for potential BIPV applications [134, 135]. Two decades of intense research in this field has yielded molecularly-engineered dyes and advanced electrolytes that have pushed the efficiencies to above 14% [136–138]. In this time the devices architecture of DSSCs has not changed significantly, with the anode still largely being glass/FTO, due in part to its high temperature stability that is required to sinter TiO_2, a mesoporous TiO_2

scaffold film still being used due to its chemical resistance, low cost and low work function, and the counter electrode (cathode) being platinum (Pt) coated FTO glass (see figure 6) [139, 140]. Notably, alternate structures using sensitized photocathodes have been also demonstrated, but the efficiencies of these lag in comparison [141].

An inherent feature and one of the major advantages of the DSSC architecture is in its semi-transparency [142]. The traditional glass/FTO/TiO_2 photoanode readily provides greater than 80% AVT at micron-level thicknesses using 10–20 nm nanoparticles [143]. Typically, high efficiency devices introduce haze within this layer through micro-structuring of the TiO_2 [144, 145], which is not conductive for semi-transparent devices. Whilst possessing appropriate transparency, a caveat of mesoporous TiO_2 photoanodes is that they contain numerous grains boundaries, which induces poor charge transport properties and, thus, lowers the achievable device performance [145]. A host of alternative anode materials, processing steps and treatments have been investigated over the years to achieve higher transparency and efficiency. Whilst we point the readers to a number of excellent reviews in this area [146–148], some key aspects can be drawn from these: (i) departing from FTO to a more transparent TCO (e.g. AZO) can provide improved photocurrents [146]; (ii) controlling of pores and microstructure is an inherent necessity towards optimising transparency [145]; and (iii) providing better alignment between the anode and the sensitiser through doping (e.g. F [149], I [150], Cu [151]), interfacial modification by small molecules (e.g. 1-decylphosphonic acid [152] and hexadecylmalonic acid [153]) or alternative anode material selection (e.g. ZnO [154], Nb_2O_3 [155]) are necessary to reduce voltage losses stemming from electronic level mis-alignment.

The counter-electrode has traditionally played the important role of catalyzing the reduction of the oxidized charge mediator [156]. By nature of the chemical stability required for this, Pt has been the most used electrode coating. One of the most common methods to deposit Pt is through thermal decomposition of the complex H_2PtCl_4. This yields thin Pt coatings with visible transmittance values of more than 80% [157]. Pt nanoparticles deposited as thin coatings from solution are also suitable, providing visible transmittance values approaching 90% [157]. Both of these provide sufficient transparency for semi-transparent application; however, it has been shown that thin platinum coatings corrode within the I^-/I_3^- redox electrolyte [158]. For this reason, sputtered Pt layers that are 0.2–2 μm thick are typically used to provide long term stability, with such layers possessing an AVT of less than 10%. Evidently, for semi-transparent applications shifting to inherently semi-transparent electrode modifiers and/or to less corrosive redox couples are critical.

A number of materials have been assessed as potential replacements of Pt in DSSC [159–161], including: polyaniline (PANI) [162, 163]; PEDOT [160, 164]; graphene [165–167]; and CoS [168]. PANI is particularly interesting because of its good electrocatalytic behaviour, low-cost and stability [162]. Bifacial devices fabricated with PANI counter electrodes and an I^-/I_3^- redox couple have exhibited PCEs of 6.7% and 4.15% under front and back illumination, respectively [163]. The PANI counter electrode in these instance possessed transmittance values as high as 70% in the visible to enable appreciable performance through the back contact. Through the use of poly(vinyl pyrrolidone) (PVP)/PANI composites, Jing *et al* further showed that a more homogenous PANI nanoparticle coating could be achieved with improved adhesion of the composite film to the substrate. Compared with Pt counter electrodes, such PVP/PANI composite films provided greater transparency, stability and yielded back illumination efficiencies that were 85% of the front [169]. Whilst PANI exhibits reasonable transparency across the visible region, significant improvements are still required to minimise optical losses for semi-transparent applications.

In addition to research into Pt alternatives, moving beyond volatile liquid electrolytes remains a key challenge for DSSC integration due to their stability, toxicity and leakage issues [170]. A variety of ionic liquids (e.g. 1-ethyl-3-methylimidazolium tetrafluoroborate) and quasi-solid-state electrolyte polymer gels (e.g. poly(ethylene oxide) or polymethylmethacrylate, PMMA, impregnated redox couples) have been assessed as alternatives [171]. Although the scalability benefits of these have been demonstrated on large scale DSSCs with a transmittance of 50% across the visible range [163], the liquid nature across these has still presented problems due to leakage [172]. Moving to all solid-state conductors remains the major challenge for practical devices. Bach *et al* were the first to demonstrate a solid-state DSSC when they replaced the conventionally used I^-/I_3^- liquid electrolyte with 2,2′,7,7′-tetrakis-(N,N-di-p-methoxyphenylamine)-9,9′-spirobifluorene (spiro-OMeTED) [173]. Spiro-OMeTED has since become the archetypal hole-transport materials for various solid-state technologies, including those based on the recently developed perovskite structures, for which PCEs exceeding 15% have been demonstrated [30, 174]. Due to its high cost and stability concerns, numerous alternatives to spiro-OMeTED are currently being investigated (e.g. PEDOT [175], polyfluorenes [175], CuI [176], CuSCN [177], NiO [178]), although to date it still remains the best hole transport candidate.

Summing all of the above contributions highlights that the underlying DSSC structure without any sensitizers can readily exhibit a transmission of >60% across the visible. Of all the sensitizers available (e.g. dyes, quantum dots, inorganics) [147], dyes provide the most flexibility for semi-transparent solar cells as these are Gaussian absorbers and their optical absorption can, in principle, be tuned to possess visible semi-transparency, whilst absorbing in the IR [179]. Ruthenium-containing complexes, metallated porphyrins and their analogues, and metal-free donor–acceptors represent the three major classes of dyes that have been successfully investigated for high efficiency DSSC [174]. Of these, the more traditional metal containing dyes, such as di-tetrabutylammonium cis-bis(isothiocyanato)bis(2,2′-bipyridyl-4,4′-dicarboxylato) ruthenium(II) (N719), have been widely reported to exhibit efficiencies of up to 10%. With strong absorption within the visible, the AVT is less than 10% for such systems at these efficiencies [180]. Synthesis of alternate absorbers has largely been focussed on systems that are compatible with the I^-/I_3^-

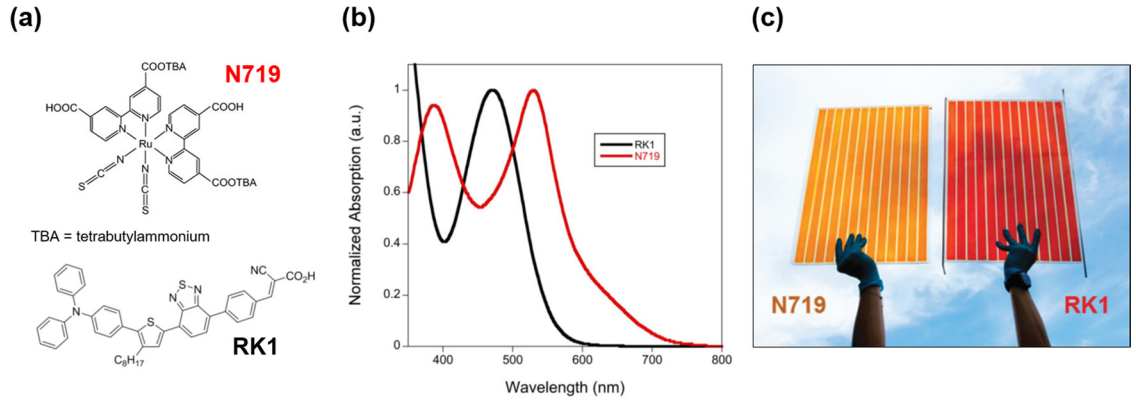

Figure 9. (a) Chemical structures of the ruthenium N719 and metal-free RK1 dyes. (b) Absorption spectra of the dyes in CH_2Cl_2. Reprinted with permission from [183]. © 2014, Nature. (c) Photograph of the large area solar panels with RK1 and N719 dyes that fabricated by Solaronix. Reprinted with permission from [181]. © 2015, Royal Society of Chemistry.

redox couple, which has historically been the only redox couple with reasonable stability [181]. These have for the most part been metallated complexes due to their stability, with functionalised porphyrins recently emerging as lucrative candidates within a Co^{2+}/Co^{3+} redox couple [130, 131]. A promising metal-free family of functional triphenylamine-based organic dyes with a cyanoacetic acid surface complexing moiety (e.g. 2-cyano-3-(4-(7-(5-(4- (diphenylamino) phenyl)-4-octylthiophen-2-yl) benzo [c][1,2,5] thiadiazol-4-yl) phenyl) acrylic acid, RK1) have provided the necessary stability and tunability of the energy levels to optimise voltage losses with respect to the TiO_2 and the redox system to exhibit record PCE of more than 14% [138, 182, 183]. These dyes have been successfully employed in large area solar cells (1750 cm^2) that exhibited a very modest power output of 10.5 W m^{-2} and an overall PCE of only ~1% (figure 9) [181]. Dyes that are optimised for IR absorption are less developed for DSSCs, although examples provided by zinc pthalocyanine derivatives [184], boron-dipyrrins [185], and unsymmetrical squaraines [186], clearly demonstrate the possibilities. Developing high-efficiency dyes that are designed for transparency in the visible and provide PCEs approaching 10% remains an opportunity for DSSCs.

3.6. Organohalide perovskites

Semiconducting organohalide perovskites have the form $A^{(1+)}B^{(2+)}X_3^{(-1)}$, where A represents large monovalent cations (e.g. $CH_3NH_4^+$, $HC(NH_2)_2^+$ or Cs^+) [187], B are large divalent metal ions (e.g Pb^{2+} or Sn^{2+}) [188] and C being monovalent halide anion (e.g. Cl^-, Br^-, I^-). Discovered in the latter part of the 19th century [189, 190], these materials have only recently emerged as one of the most promising next-generation photovoltaic candidates [191–194]. Originally trialled within sensitized solar cell structures, for which initial PCEs of 3.8% were noted [195], the first true promise arose when spiro-OMeTAD was used to develop 'superstrate' perovskite solar cell (PSC) configurations and a PCE of 9.7% was achieved [196]. Tremendous research efforts into perovskites have since ensued, which have yielded certified PCEs of 22.1%, with $J_{sc} = 24.97$ mA cm^{-2}, $V_{oc} = 1.105$ V and FF of 0.803 [31]. This success can be ascribed directly to their composition-dependent, tunable and direct optical bandgaps, large light absorption coefficients, high carrier mobilities and long carrier diffusion lengths [197, 198].

Investigations into semi-transparent PSCs began with the milestone work by the Snaith group in 2014, who realized a colour-neutral, semi-transparent PSC with a PCE of 3.5% and an AVT of 30% [199]. The authors made use of the perovskites partially de-wetting to form microstructured arrays of perovskite 'islands', which were thick enough to absorb all visible light, while the voids enabled the transparency. The device structure consisted of glass/FTO/compact-TiO_2/perovskite/spiro-OMeTAD/Au, where the 10 nm thick gold electrode was thermal evaporated (see figure 10). The AVT was linearly dependent on perovskite surface coverage (figures 10(b) and (e)). By nature of the absorber islands, shunting paths between the active layer led to low V_{oc} and FF compared to the densely coated films. In view of this problem, electrically insulating long alkyl chain silane molecules (octadecylsiloxane) were introduced within the perovskite island layer as a shunt-blocking component [200]. With this treatment, the shunt resistance significantly increased and the PCE improved to 6.1% at an AVT of 38%.

Another effective way to fabricate semi-transparent PSCs is to thin the perovskite layer and engineer the electrodes for maximum transparency. One of the most versatile approaches towards engineering transparent electrodes is through the use of dielectric–metal–dielectric (DMD) stacks [201]. By independently controlling the thickness of each layer in the stack, these structures enable the electric field across the entire device to be optimized for transmission. In our previous work, MoO_x/Au/MoO_x stacks were used as top electrodes on normal PSC architectures (see figures 11(a)–(c)) [48]. MoO_x was used in this stack because it provides the well-established hole injection properties, while also acting as a good wetting surface for depositing thin and uniform Au films. The latter was critical towards achieving high transparency through the stack due to the avoidance of plasmonic features (figures 11(d)–(f)). As for gold, it provided the conducting element, while offering excellent stability towards air oxidation and corrosion resistance towards halides. Optimized devices demonstrated PCEs

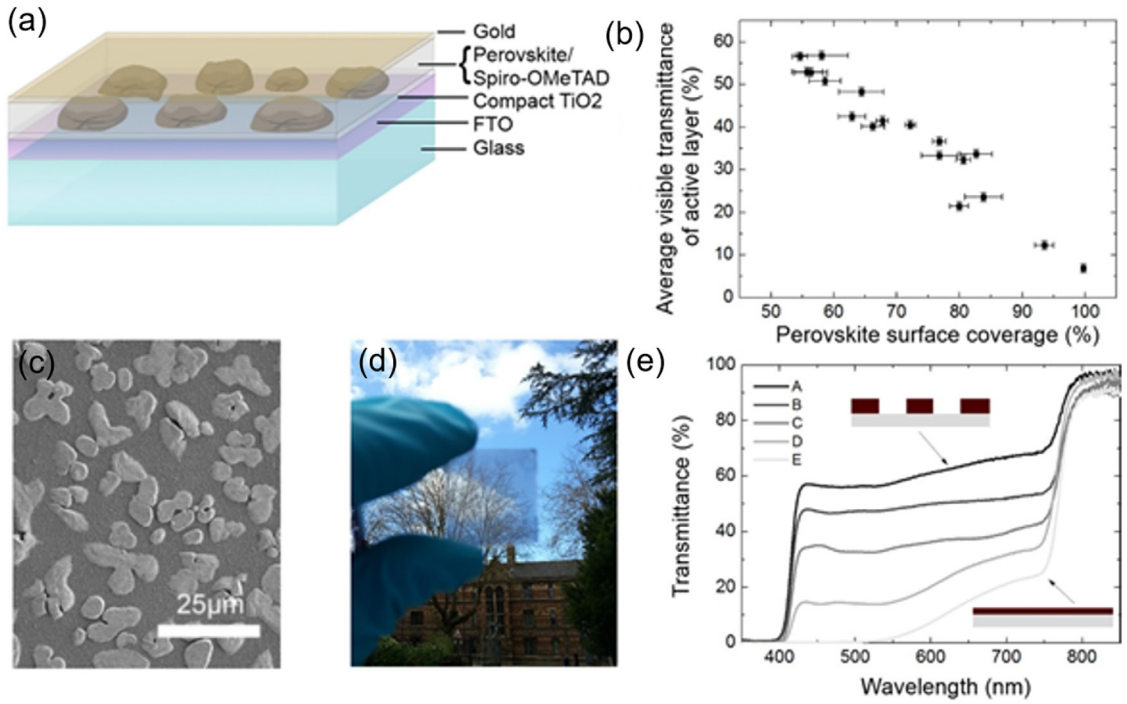

Figure 10. (a) Diagram showing the architecture of the de-wet planar perovskite heterojunction solar cell. (b) Dependence of AVT of the active layer on perovskite surface coverage. (c) Scanning electron micrograph of the top surface of a representative film of perovskite islands (paler regions) on a TiO_2-coated FTO substrate. (d) Photograph through a typical semi-transparent perovskite film formed on glass, demonstrating neutral colour and semi-transparency. (e) Transmittance spectra of active layers of a selection of de-wet perovskite devices. Schematic representations of the most and least transparent films are shown as insets. Reproduced with permission from [199]. © 2014, American Chemical Society.

of 5.5%–13.6% at AVT values of 31%–7%, respectively. The multilayer electrode has also been harnessed in tandem solar cells by Yang's group [202]. In that work it was also found that either silver or gold monolayer at a thickness of 11 nm was non-continuous and resistive; however, through the use of an ultrathin gold seed layer, the film nucleation and growth mode (from Volmer–Weber mode to Frank-van der Merwe growth) were modified to provide continuity and high conductivity.

The replacement of spiro-OMeTED in such structures is an important step forward because it possesses high absorption within the higher energy part of the visible spectrum, it is difficult to keep stable due to its partially oxidized form, and it is extremely high in cost [203]. Many works have focused on substitutes of spiro-OMeTED that fulfil the requirements of high transparency and *p*-conductivity simultaneously, with PEDOT:PSS being one such candidate. Roldán-Carmona *et al* reported a semi-transparent inverted PSC with PEDOT:PSS hole transport layer (HTL) that achieved 6.4%–7% PCE at 29%– 22% AVT, respectively, using thermally evaporated perovskite layers [199]. The metal electrode was a 6 nm ultra-thin gold film with a LiF protective layer. Evidently, unlike the spiro-OMeTED, PEDOT:PSS served as a suitable wetting layer for ultra-thin Au. Adopting a similar structure, Jung *et al* introduced CuSCN as an alternative HTL material due to its superior transparency across the (ultraviolet–visible–near infrared) UV–vis–NIR spectrum. Adopting a similar structure, this facilitated a further improvement of the PCE to 10% with an AVT of 25% [204].

Alternative electrodes including transparent carbon materials (e.g. carbon nanotubes (CNTs) [205] and graphene [206]), metal nano-networks (e.g. Ag nanowire (NW) [50, 207, 208] and Ni mesh [209]) and conductive oxides (e.g. ITO [210–212]) have also been widely investigated as potential electrode for semi-transparent PSCs. Carbon materials are particularly advantageous because of their chemical stability and their large scale fabrication potential. Among them, CNTs are among the most interesting due to their efficient 1D electrical transport. Li *et al* were the first to demonstrate transferable CNT films as top electrodes of PSCs [205]. The use of CNTs enabled the metal electrode and hole transporting layer to be avoided, which simplified the PSC fabrication by avoiding vacuum processing, as well as the use of expensive HTL materials and noble metal electrodes. Graphene has been also widely used in photovoltaics due to its high intrinsic charge carrier mobility, good electrical conductivity and high optical transmittance [213]. Transferable multilayer graphene stacks prepared by chemical vapour deposition (CVD) were firstly laminated as top electrode by Yan's group [206]. These showed PCEs of 12.0% and 11.7% when the normal structured PSC devices were illuminated from the bottom (FTO side) and top (graphene side) electrodes, respectively. Although AVT was not provided, the comparable transmittance of Poly(dimethylsiloxane) (PDMS)/PMMA/Graphene/PEDOT:PSS was above 90% across the visible, which is sufficient to show outstanding transparency. As larger graphene sheets become commercialised, graphene electrodes will provide a facile solution towards roll-to-roll fabrication of semi-transparent PSCs [214].

Despite the great potential of carbon materials, their currently high sheet resistances (2–25 kΩ sq^{-1} for CNT and

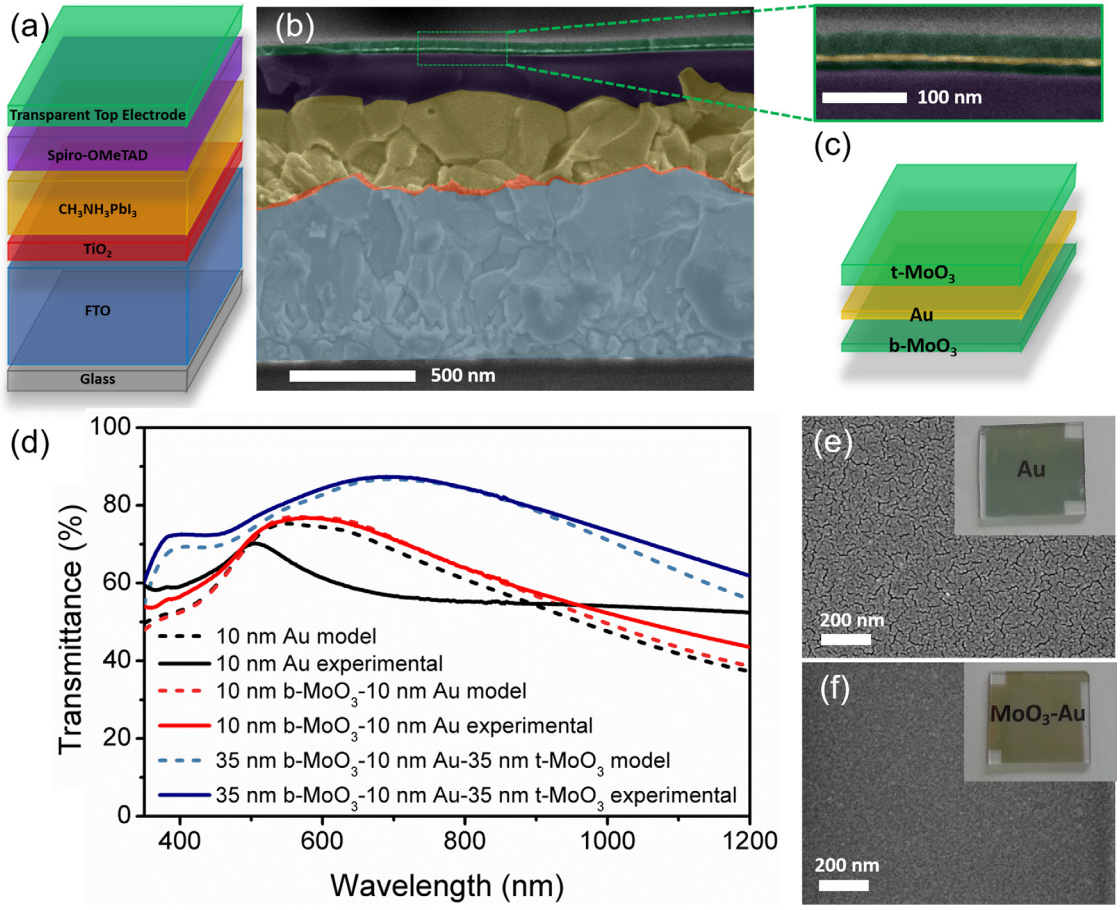

Figure 11. (a) Schematic illustration of the PSC architecture. (b) SEM image in cross section of a complete device with photo image inset of the device. (c) Enlarged view of the multilayer top electrode and schematic of its structure. (d) Simulations (shaded dashed lines) and experimental data (solid lines) showing the transmittance of Au (black), *b*-MoO_3/Au (red) and *b*-MoO_3/Au/t-MoO_3 (blue). (e) SEM image of Au film. (f) SEM image of *b*-MoO_3/Au film. The insets show photos of the two samples. Adapted with permission from [48]. © 2015, Elsevier.

1 kΩ sq^{-1} for graphene monolayer) restrict the performance of PSCs by resulting in a low FF. Metallic nano-networks, especially Ag NWs [215], have been increasingly studied as a more promising electrode for transparent PSC thanks to their solution processability, mechanical flexibility, improved electrical conductivity and higher optical transmittance compared to carbon materials [216]. Guo and co-workers reported solution-processed Ag NWs as top electrodes with a configuration of Glass/ITO/PEDOT:PSS/$CH_3NH_3PbI_{3-x}Cl_x$/$PC_{60}BM$/Ag NW (figure 12(a)). These devices exhibited a PCE of 8.49% at an AVT of 28.4% (figure 12(b)) [208]. This was the first report of solution processed Ag NWs as top electrodes within PSCs without damaging the underlying perovskite layer. The key to this progress was the introduction of a thin zinc oxide nanoparticles interlayer onto the [6,6]-phenyl-$C_{61,71}$-butyric acid methyl ester (PCBM) hole blocking layer, which acted as both a protecting layer and ensured an ohmic contact between the PCBM and Ag NWs (figure 12(c)). Despite this progress, an inherent caveat of silver is that it is high cost and is susceptible to degradation due to the halides from within the perovskite layer. As an outstanding substitute, a roll-to-roll produced nickel mesh that was embedded in a poly(ethylene terephthalate) (PET) film to provide a transparency of 86%, was laminated as a top electrode onto a PSC [209]. The nickel mesh electrode showed lateral conductivity of ca 1.2 Ω sq^{-1} and the completed device demonstrated a PCE of 13.3%, which was slightly lower than the 14.3% obtained for evaporated Au electrodes. The PCE was 9.8% when light illuminated from the nickel mesh electrode side, which highlights its excellent performance in semi-transparent bi-facial PSCs.

Undeniably, TCO electrodes are the most popular transparent electrodes at the moment because of their great optical and electrical properties. However, few works have reported TCOs as top electrodes. One of the constraints stems from the magnetron sputtering used to deposit TCOs, which damages the soft perovskite layer [211]. This can be avoided through the use of a protective layer on the perovskite film [212, 213]. For instance, Fan Fu et.al introduced an MoO_3 protection layer on spiro-OMeTED before sputtering 170 nm of In_2O_3:H as a transparent electrode and achieved a semi-transparent PSC with a PCE of 14.2% [212]. An alternate approach developed by Heo *et al* has avoided sputtering altogether through the lamination of a dried PEDOT:PSS coated ITO glass onto a wet HTL/$MAPbI_3$/TiO_2/FTO substrate [210]. The AVT of completed devices ranged from 17.3% to 6.3%, with the corresponding average PCE ranging from 12.6% to 15.8%, respectively.

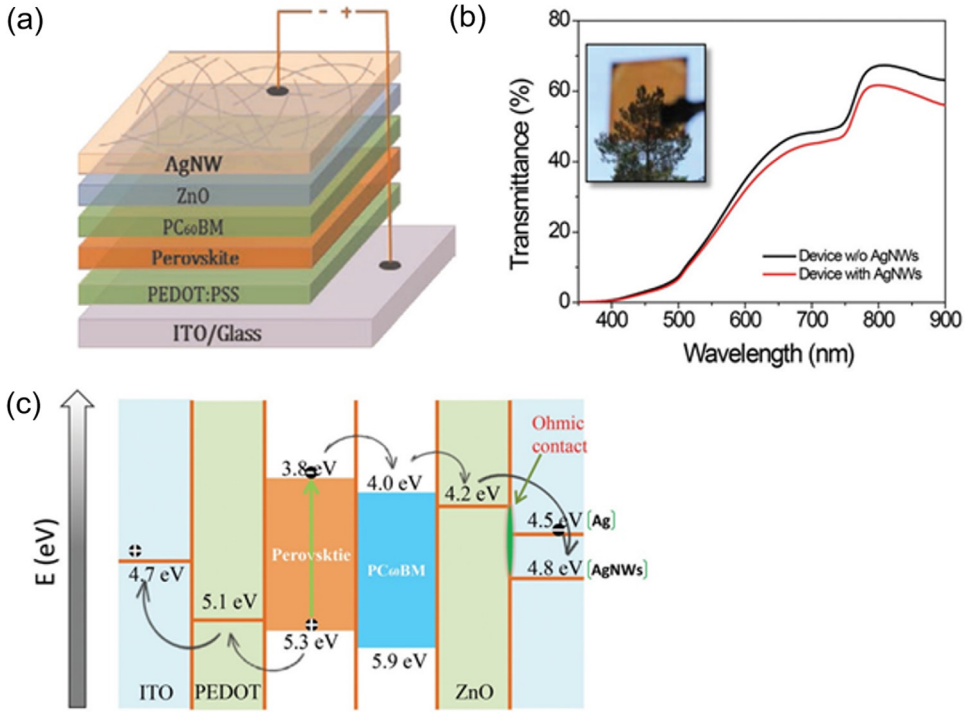

Figure 12. (a) Schematic structure of the devices with solution-processed top AgNWs. (b) Transmittance spectra of the device without and with AgNW top electrodes, which were measured before and after AgNWs deposition. The inset shows the photo of a complete semi-transparent device. (c) Energy diagram of the devices with a ZnO layer between $PC_{60}BM$ and Ag (or AgNWs). Reproduced with permission from reference [208]. © 2014, Royal Society of Chemistry.

The progress made in the efficiency of PSCs is unparalleled by any other semi-transparent technology. However, these materials are still very much at the research phase because of two major problems that need to be resolved prior to any deployment: (i) stability and (ii) toxicity. The archetypal $MAPbX_3$ is well known to suffer from degradation in air and moisture. This has triggered significant research efforts towards encapsulation technology and finding stable methyl ammonium substitutes, such as cesium and formamidinium [217–219]. Toxicity stems from the water-soluble lead that is contained within all high efficiency perovskite materials to date. Encouraging progress has been made towards developing PSCs with non-toxic candidates, such as formamidinium tin iodide; however, the efficiencies of such devices are not yet comparable to their lead-based analogues [220, 221]. It is fair to say that this research area is in its early stages, and these challenges will likely be solved in the not too distant future.

3.7. Organic photovoltaics

Organic photovoltaics (OPV) can be characterised among two main classes: (i) evaporated small-molecule systems and (ii) blends of donor-accept small molecules and/or polymers, which are known as BHJ. Developed in 1984 by Tang [26] and in 1994 by Yu *et al* [27], respectively, these devices possess many of the same spectral-engineering advantages as DSSCs [222], but, because they are inherently solid-state and can be fabricated with semi-conducting polymers, which are more amenable to scalable production [223]. OPVs generally possess 'superstrate' device structures within 'normal' or 'inverted' configurations, these being where the electrodes preferentially enable hole or electron extraction, respectively, through to the glass/TCE electrode [224]. Of the thousands of various candidates that have been assessed in this broad field, highly engineering poly[(5,6-difluoro-2,1,3-benzothiadiazol-4,7-diyl)-alt-(3,3‴-di(2-octyldodecyl)-2,2′;5′,2″;5″,2‴-quaterthiophen-5,5‴-diyl)] (PffBT4T-2OD) as donors and [6,6]-2-Thienyl-C_{71}-butyric acid methyl ester ($TC_{71}BM$) as acceptors within BHJ structures have yielded the highest PCEs among single-junction opaque OPV devices of 10.8%, with $J_{sc} = 18.8$ mA cm^{-2}, $V_{oc} = 0.77$ V and FF of 0.75 [225]. In addition to these advances in opaque OPV, semi-transparent devices have attracted great interest throughout their history due to the tuneable molecular structures [226]. An enormous amount of work has been carried out in this space, with a recent review into such devices having been reported elsewhere [227]. As such, here we will only cover the state-of-the art devices for completeness.

The workhorse OPV system was for many years poly(3-hexylthiophene) (P3HT) and PCBM BHJ, which provides reasonable efficiencies of 3–4% and is relatively stable [228]. For semi-transparent applications, the relatively low PCE of this system and the visible optical bandgap of P3HT (~2.2 eV), has motivated significant efforts to develop low-bandgap donor polymers to preferably absorb NIR and UV light, while still operating with derivatives of C_{60} or C_{70} as acceptors [229]. Of these, the group of Jen reported among the best semi-transparent devices using the donorpolymers:2,6-Bis(trimethyltin)-4,8-bis(5-(2-ethylhexyl) thiophen-2-yl)benzo[1,2-b:4,5-b']dithiophene (PBDTTT-C-T,

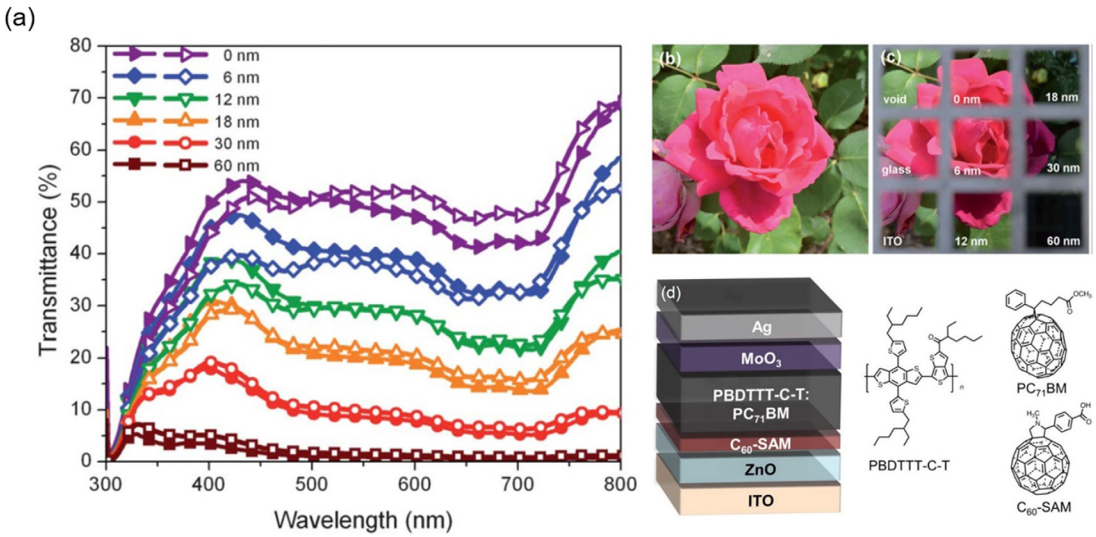

Figure 13. (a) Transmission spectrum of the semi-transparent OPV devices from optical modeling (closed symbols) and the real devices (open symbols). (b) and (c) Photographs of a pink rose taken with exactly the same camera settings (shutter, aperture, white balance, etc) on a sunny day. (d) Device architecture of inverted cells and the chemical structures of the active materials PBDTTT-C-T and $PC_{71}BM$ and the self-assembled molecule C_{60}-SAM. Reproduced with permission from [230]. © 2012, Royal Society of Chemistry.

band gap of ~1.9 eV) [230], poly(indacenodithiophene-co-phenanthro[9,10-b]quinoxaline) (poly (PIDT-PhanQ), band gap of ~1.7 eV) [231] and F-containing poly[2,6-(4,4-bis-(2-ethylhexyl)-4H-cyclopenta[2,1-b;3,4-b]dithiophene)-alt-4,7-(2,1,3-benzothiadiazole)] (F-PCPDTBT, band gap of <1.7 eV) [232]. The champion BHJ devices used PBDTTT-C-T/$PC_{71}BM$ donor/acceptor blends and showed an AVT up to 40% with a PCE of ~5% when the thickness of a Ag top electrode was optimised (see figure 13). Meanwhile, the group of Yang focussed on alternating diketopyrrolopyrrole (DPP) and thienylbenzodithiophene (BDTT) copolymers, within which they copolymerised furan-, thiophene- [233] and selenophene- [234] containing DPP units. Switching the furan to a thiophene or selenophene moiety in this polymer reduced the optical bandgap progressively from 1.51 eV to 1.46 eV then 1.38 eV, respectively. Due to the extended spectral absorption, the selonophene-based polymer possessed the best semi-transparent OPVs with a PCE of ~4.5% at a corresponding AVT of ~60%.

Whilst polymers possess the ease of solution-processing, small molecule photoactive materials possess more defined molecular structures, which result in less batch-to-batch variation and greater control of energy levels [235]. Through molecular engineering, numerous donor (e.g. benzannulated difluoro-bora-bis-(1-phenyl-indoyl)-azamethine (Ph_2-benz-bodipy) [236] and phthalocyanine derivatives [237–239]) and acceptor (e.g. C_{60} [237], 3,4,9,10-perylenetetracarboxylic bis-benzimidazole (PTCBI) [239]) systems have been identified with suitable absorption properties for use in semi-transparent devices. For example, Lunt *et al* reported evaporated small molecular chloroaluminium phthalocyanine (ClAlPc) and C_{60} bi-layered OPV. Using ITO as both a front and back electrode, with appropriate hole (MoO_x) and electron (bathocuproine) injection layers, OPVs were fabricated with a PCE of 1.3% at an AVT of 65% [237]. Incorporation of a broad-band anti-reflection (BBAR) coating optimised for the infrared further improved the PCE of this device structure to 1.7%, with only a marginal reduction of AVT to 56%. Alternate systems, such as Ph_2-benz-bodipy (absorption peak at ~773 nm) [236] and ZnPc (absorption peak at ~670 nm) [238] blended with C_{60} have yield more favourable PCE values of ~2.2% at AVTs of more than 40%. Whilst these lucrative AVT values fulfil the visual requirement of BIPV, the overall performance of small-molecule semi-transparent devices are rather poor, particularly compared to their polymer counterparts. Interestingly, progress into opaque small molecule OPVs has achieved PCEs of over 10% [240]; however, the difficulty in depositing high-quality thin-films from such materials, particularly from solution, has restricted progress for their semi-transparent counter-parts [235].

Many of the above devices use ultra-thin metal layers as electrodes, which are known to possess non-optimal transmission properties. An alternative approach to improve the transmittance was developed by Choy's group, who introduced a metal/nanoparticle/dielectric electrode structure containing Si nanoparticles to induce scatter and a Tris (8-hydroxyquinolinato) aluminium (Alq_3) index matching layer on top of ultra-thin Ag [241]. Within this structure, solar cells using DPP:$PC_{71}BM$ BHJs exhibited an overall AVT of 32%, with an appreciable PCE of 6.22%. DMD multilayer TCEs have been more typical in OPV to achieve optimal transmittance [230], with examples including: MoO_3/Ag/MoO_3 [242], ZnS/Ag/WO_3 [243], MoO_3/Ag/WO_3 [244], MO_3/Ag/V_2O_5 [245] and ZTO/Ag/ZTO [246]. Such electrodes exhibit AVTs ranging from 60 to 80%, with sheet resistances as low as 5 Ω sq^{-1}; however, device PCEs have typically been relatively low at 1–3% owing to the use of P3HT:PCBM BHJs among most of the examples.

DMD structures are highly lucrative, but are realistically limited to evaporation methods for their deposition. To achieve all-solution-processing of OPVs, which is highly desirable from a production perspective, alternative electrodes and processes must be used [247–250]. A number of solution-processed

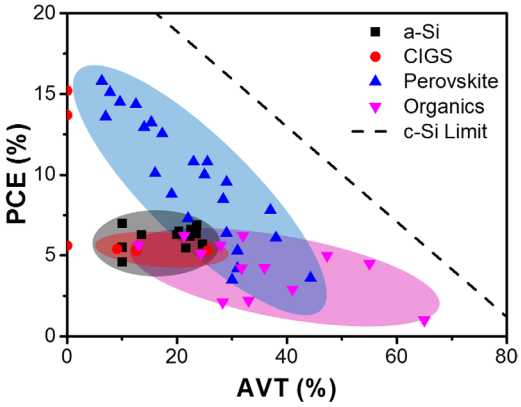

Figure 14. Summarized PCE and AVT plots of the various semi-transparent solar cell technologies assessed in this review. For clarity, the different device classes have been highlighted with the corresponding symbol colours. Detailed data are showed in table 1 with accompanying references. The *c*-Si limit presents the practical limits of semi-opaque devices produced using cells with record efficiencies of 25%. It should be noted that when AVT is 0, the devices are bifacial.

TCEs have been investigated within semi-transparent OPVs, including CNT [251] and PEDOT:PSS [51, 252, 253]. These electrodes generally resulted in PCE values of ~2% at AVTs of ~20% for P3HT:PCBM BHJs. The challenges with these electrodes are the relatively high sheet resistances (>100 Ω sq^{-1}) compared to DMD structures. An elegant alternative approach that overcomes these factors is through lamination of pre-fabricated electrode structures. Laminated semi-transparent OPVs were firstly reported by Huang in 2007, who used Cs_2CO_3 as a buffer layer to lower the work-function of an ITO cathode, and D-sorbitol modified PEDOT:PSS as a conducting polymer glue with an ITO anode electrode for lamination [254]. Using a P3HT:PCBM BHJ the devices exhibited PCE values of ~3% with an AVT of ~15%. Brabec *et al* improved on these devices by using ITO/Ag/ITO on PET as a bottom electrode and Ag NWs on PET, with a PEDOT:PSS and D-sorbitol transparent conducting adhesive, as a top electrode [255]. The authors achieved record PCE values of 5.3% for PBTZT-stat-BDTT-8:PCBM BHJs at an AVT of 31%.

Overall, the above assessment of the semi-transparent OPV field demonstrates very promising PCE values for a variety of BHJ systems. While OPVs possess lower efficiencies compared to most other opaque thin-film solar cells [256], for high AVT values (>40%) they actually exhibit the best PCEs (see figure 14). This directly stems from both advanced molecular-engineering and optimisation of TCEs to exhibit high visible transparency. Further improvements to the performance of semi-transparent OPVs can be made, but will require overcoming the inherent voltage losses that plague OPV [257] and enhancing the relatively low charge mobilities [222].

4. Challenges and future opportunities

In this review we have provided an overview into the developments of all the major semi-transparent solar cell classes that have been demonstrated to date. Of these, amorphous silicon devices remain the most widely deployed, which largely stems from their longer development history compared to the other candidates. However, these devices have effectively stagnated in their device performance, thus creating an opportunity for emerging material classes. This is clearly demonstrated in table 1 and figure 14, where we compare the best efficiencies for the different semi-transparent technologies versus their AVT. The amorphous silicon benchmark efficiency is ~5% at ~10–20% AVT. Most of the emerging candidates that have been discussed in this work have already demonstrated comparable, if not higher, efficiencies than this. Of these, perovskites clearly present one of the greatest opportunities, with efficiencies of prototype, small-scale devices nearly doubling that achievable from commercial amorphous silicon devices.

From a theoretical perspective, the overall performance of semi-transparent devices can be further improved. Lunt determined the Shockley–Queisser (SQ) limit for single-junction PVs that were made with a modified transmittance only across the visible region (see figure 15) [258]. The results showed that the SQ efficiency linearly decreased from 33.1% for opaque devices to 20.6% when there was no visible light absorption, with an accompanying optimal bandgap redshift from 1.36 eV to 1.12 eV. These trends provide practical OPV efficiency limits of ~17% to ~10% at 0%–100% AVT, respectively. Strictly speaking these results are valid only for OPVs, which can be engineered to absorb in the IR and be mostly transparent in the visible. For semi-opaque devices, the predicted efficiency linearly decreases to 0% for 100% visible transmittance. Given that the theoretical efficiency limit of $CH_3NH_3PbI_3$ PSCs is ~31% [259] and the current record efficiency is ~22% [31], it can be readily deduced from this figure that superior efficiencies will be achieved for PSCs versus OPVs at AVT values of less than ~40%; however, at higher transparencies, OPVs should be a more viable option. This prediction is consistent with the best-in-class PCE values for perovskite and OPV devices reported to date. Notably, the practical limit for double-glazed, semi-opaque solar cells with tiled *c*-Si cells that possess record cell efficiencies of 25% remain comparatively higher for every AVT (see figure 14). Although this difference represents the current efficiency cost of semi-transparency, it will undoubtedly reduce with further improvements to semi-transparent devices.

Based on the above analysis, it is clear that most emerging semi-transparent classes are already at commercial-ready levels. However, such devices have to be considered from a number of additional facets, including toxicity, stability, mechanical properties, aesthetics and processability. Most of the emerging material candidates can be considered non-toxic. The most notable exceptions are CdTe and the perovskites, which currently all use water soluble lead species (e.g. methylammonium lead iodide). Building products are highly regulated, particularly around toxicity. Therefore, unless the toxicity issues are resolved, it is unlikely that such products will be permitted for building integration in any form. The high efficiencies of the lead-based perovskites in both opaque and semi-transparent device structures have created a particular global focus on finding an alternative material that is non-toxic and exhibits comparable device characteristics [191].

Table 1. Summary of semi-transparent properties.

Active Materials	Electrodes (anode)	Electrodes (cathode)	Configuration (from normal illumination side)	AVT (%)	PCE (%)	Reference
Amorphous Si	N/A	N/A	N/A	10	7	[263]
Amorphous Si	N/A	N/A	N/A	10	4.6	Kaneka
				10	5.5	Corporation
a-Si:H	Gallium-doped zinc oxide (GZO)	GZO	Glass/GZO/*n–i–p a*-Si:H/high-bandgap layers/GZO	24.6	5.71	[65]
				22.3	6.21	
				22.5	6.64	
				23.5	6.33	
				20.3	6.53	
				23.6	6.92	
a-Si:H	GZO glass	GZO	Glass/GZO/*n–i–p a*-Si:H/GZO	20.8	4.65	[66]
				21.7	5.55	
				21.6	5.46	
				19.2	5.58	
a-SiGe:H	GZO glass	GZO	Glass/GZO/*n–i–p a*-SiGe:H/GZO	17.9	17.9	[66]
N713	FTO glass	Pt	Glass/FTO/TiO_2/N713/Pt	53.68	3.26	[264]
N3:PMMA	FTO glass	Pt	Glass/FTO/TiO_2/N3:PMMA/Pt	50	1	[170]
N719	ITO/AZO film	Pt PET	ITO/AZO/ZnO NW/N719/photoresist/Pt/PET	40	0.27	[265]
D-358	ITO glass	Pt	ITO/ZnO/D-358/Pt	N/A $T_{>550nm}$ = ~30	5.9	[266]
N3	FTO glass	PANI	Glass/FTO/TiO_2/N3/PANI	N/A Bifacial	Front:6.54 Rear:4.26	[162]
N719	FTO glass	PANI/FTO glass	Glass/FTO/TiO_2/N3/PANI/FTO Glass	N/A Bifacial	Front:6.70 Rear:4.15	[163]
RK	FTO glass	Pt	Glass/FTO/TiO_2/RK/Pt	N/A $T_{600–1000nm}$ = ~50	5.75–7.36	[181]
CIGS	ITO/SLG	ZnO:Al	SLG/ITO/CIGS/CdS/*i*-ZnO/ZnO:Al	25.5	5.27	[87]
				12.6	5.34	
				9.1	5.38	
CIGS	ITO/SLG	ZnO:Al	SLG/ITO/CIGS/CdS/*i*-ZnO/ZnO:Al	0	12.6	[78]
$CH_3NH_3PbI_3$ island	FTO glass	Au	Glass/FTO/ TiO_2/$MAPbI_3$ island/spiro-OMeTAD/Au	30	3.5	[199]
$CH_3NH_3PbI_3$ island	FTO glass	Au	Glass/FTO/TiO_2/$MAPbI_3$ island/Octadecyl-trichloro silane/spiro-OMeTAD/Au	38	6.1	[200]
$CH_3NH_3PbI_3$	ITO glass	Au	Glass/ITO/PEDOT:PSS/$MAPbI_3$/PCBM/Au/LiF	29	6.4	[203]
				22	7.3	
$CH_3NH_3PbI_3$	Ag	ITO glass	ITO glass/CuSCN/$CH_3NH_3PbI_3$/PCBM/Ag	25	10	[204]
$CH_3NH_3PbI_{3-x}Cl_x$	FTO glass	Graphene	Glass/FTO/compact TiO_2/$CH_3NH_3PbI_{3-x}Cl_x$/Spiro-OMeTAD/PDMS/PMMA/Graphene	N/A $T_{700\ nm}$ = 22.5	11.27	[207]
$CH_3NH_3PbI_{3-x}Cl_x$	Ag NW	ITO glass	ITO glass/PEDOT:PSS / $CH_3NH_3PbI_{3-x}Cl_x$ /$PC_{60}BM$/ZnO/Ag NW	28.4	8.49	[208]
$CH_3NH_3PbI_{3-x}Cl_x$	Ag NW	ITO glass	ITO glass/PEDOT:PSS / $CH_3NH_3PbI_{3-x}Cl_x$ /$PC_{60}BM$/ZnO/Ag NW	37	7.81	[215]
				29	9.55	
				23	10.81	
				14	12.95	
$CH_3NH_3PbI_3$	Ag NW	ITO glass	ITO Glass/PEDOT:PSS / $CH_3NH_3PbI_3$/ALD ZnO/Ag NW/ALD Al_2O_3-coated PET	25.5	10.8	[267]
$CH_3NH_3PbI_3$	Ag NW	ITO glass	ITO glass/PEDOT:PSS / $CH_3NH_3PbI_3$/$PC_{60}BM$/ZnO/Ag NW/dielectric mirrors	44.3	3.6	[101]
				31	4.2	
$CH_3NH_3PbI_{3-x}Cl_x$	FTO glass	Ni mesh	Glass/FTO/TiO_2/Al_2O_3/$CH_3NH_3PbI_{3-x}Cl_x$Spiro-OMeTAD/PEDOT:PSS/Ni mesh/PET	N/A Bifacial	Front:13.3 Rear:9.8	[209]

(*Continued*)

Table 1. (*Continued*)

Active Materials	Electrodes (anode)	Electrodes (cathode)	Configuration (from normal illumination side)	AVT (%)	PCE (%)	Reference
$CH_3NH_3PbI_3$	FTO glass	MoO_3/Au/ MoO_3	Glass/FTO/TiO_2/$MAPbI_3$/ Spiro-OMeTAD/MoO_3–Au–MoO_3	31 19 16 7	5.3 8.8 10.1 13.6	[48]
$CH_3NH_3PbI_3$	FTO glass	ITO glass	Glass/FTO/TiO_2/$CH_3NH_3PbI_3$/HTL with PEDOT/ITO glass	17.3 15.3 12.5 9.6 7.8 6.3	12.55 13.25 14.35 14.5 15.1 15.8	[210]
$CH_3NH_3PbI_3$	FTO glass	In_2O_3:H	Glass/FTO/ZnO/PCBM/$CH_3NH_3PbI_3$/Spiro-OMeTAD/MoO_3/In_2O_3:H	N/A $T_{NIR} = 72$	14.5	[212]
P3HT:PC_{60}BM	Conducting plastic	Conducting plastic	Conducting plastic/Cs_2CO_3/ active layer/conducting plastic with adhesive glue	N/A $T_{600–1000\ nm} = 70$	3	[254]
PSBTBT:PC_{71}BM	ITO glass	Ag	ITO glass/ZnO/C_{60}-SAM/ PBDTTT-C-T:PC_{71}BM/ MoO_3/Ag	21.3 27.9 35.9	6.22 5.62 4.25	[230]
PIDT-PhanQ: PC_{71}BM	Ag	ITO glass	ITO glass/PEDOT:PSS/ PIDT-PhanQ: PC_{71}BM/Fullerene-containing Surfactant/Ag	13.03 24.35 31.71	5.63 5.10 4.22	[231]
PCPDTFBT-C-T:PC_{71}BM	ITO Glass	Ag	ITO Glass/ZnO/C_{60}-SAM/ PCPDTFBT-C-T:PC_{71}BM/ modified PEDOT:PSS/Ag	47.3	5.0	[232]
PBDTT-SeDPP:PC_{61}BM	Ag NW	ITO glass	ITO Glass/PEDOT:PSS/PBDTT-SeDPP:PC_{61}BM/TiO_2/AgNW	~55	4.5	[234]
P3HT:Si-PCPDTBT:PCBM	Ag NW	Ag NW	Ag NW/AZO/P3HT:Si-PCPDTBT:PCBM/PEDOT:PSS/Ag N′W	33	2.2	[247]
P3HT: PC_{70}BM	ITO glass	ZnS/Ag/WO_3	ITO Glass/Cs_2CO_3/P3HT: PC_{70}BM/ WO_3/Ag/ZnS	28.3	2.1	[243]
DPP:PC_{71}BM	ITO glass	Alq_3/Si nanoparticles/ Ag Film	ITO Glass/ZnO/DPP:P_{71}CBM/MoO_3/ Hybrid electrode	32	6.22	[241]
P3HT:PCBM	Ag NW	PEDOT:PSS (PH1000)/GO	Ag NW/TiO_x/ZnO/ P3HT: PCBM/PEDOT:PSS(Al4083)/ GO:PEDOT:PSS (PH1000)	N/A $T_{(650\ nm–1200nm)} = \sim 55$	2.3	[268]
DPP:PCBM	Ag NW	Ag NW	Ag NW/PEDOT:PSS /DPP:PCBM/ ZnO/Ag NW	41	2.9	[269]
Copper phthalocyanine (CuPc)/C_{60}	Ag NW	ITO glass	ITO/CuPc/C_{60}/Bathocuproine (BCP)/ Ag NW	26	0.63	[270]
PCDTBT:PC_{71}BM	AZO	ITO glass	ITO glass/PEDOT:PSS/ PCDTBT:PC_{71}BM/TiO_x/Al/AZO	N/A $AT_{(300–1300nm)} = 34$	3.9	[271]
Cy7-P/C_{60}	Alq_3/Ag/Alq_3	ITO glass	ITO Glass/PEDOT:PSS/Cy7-P/C_{60}/ Alq_3/Ag/Alq_3	65	1	[256]
ClAlPc-C_{60}	ITO glass	ITO glass	BBAR/Quartz/ITO/MoO_3/ClAlPc-C_{60}/BCP/ITO/distributed Bragg reflector (DBR)/BBAR	55	1.7	[237]
Ph_2-benz-bodipy-C_{60}	ITO glass	Ag/Alq_3	ITO glass/NDN1:C_{60}:Ph_2-benz-bodipy:P-doped 9,9-bis[4-(N,N-bis-biphenyl-4-yl-amino)phenyl]-9H-fluorene (BPAPF)/ Ag/Alq_3	47.9	2.2	[236]
PTCBI/CuPc	Ag	ITO glass	ITO glass/PTCBI/CuPc/BCP/Ag	60	0.28	[239]

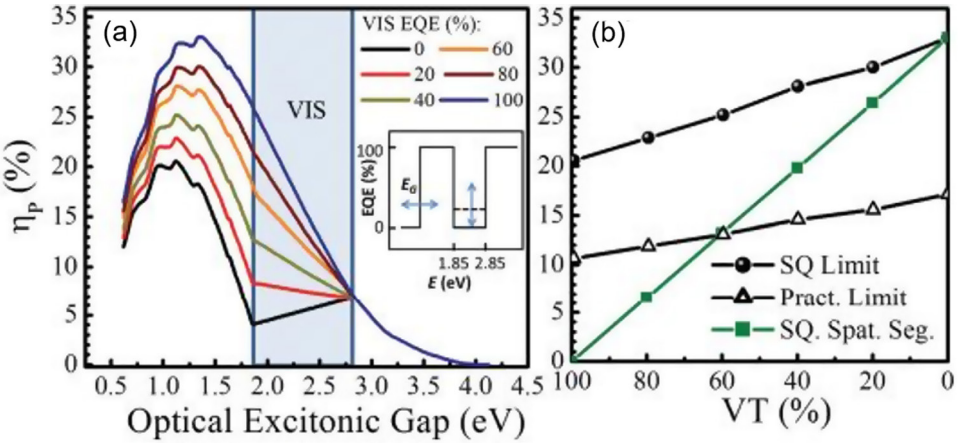

Figure 15. (a) Calculated thermodynamic limiting efficiencies for single-junction (single-bandgap) photovoltaics as a function of bandgap for transparent and semi-transparent architectures with varied EQE contributions from the visible part of the spectrum. Note that the decrease in efficiency through the visible region for 0% VIS EQE (black line) stems from the reduced open-circuit voltage combined with the lack of additional photocurrent. (b) Maximum single- junction efficiencies as a function of the total level of visible transparency in the SQ thermodynamic (closed circles), practical (open triangles), and SQ spatially segmented visibly opaque (closed squares) junction limits. The corresponding relationship between the visible EQE contribution and weighted VT can be approximated by EQE + VT = 1 in the absence of reflection losses. Reproduced with permission from [258]. © 2012, American Institute of Physics.

Apart from meeting toxicity regulations for building products, devices will additionally require stability factors of at least 10 years [25]. The chalcogen-based inorganic systems have a particular advantage in this regard as they have proven material stabilities of decades [132, 260]. Of the remaining semi-transparent systems, there are few that actually meet these requirements at this point [156, 261]. Continuing research around materials and device structures are required to understand the root causes of instability for particular systems. One of the advantages of window integrated devices is that they are exposed to much lower average irradiances compared to rooftops and, thus, will inherently possess higher comparable temporal photo-stabilities. This is a major advantage from a technological deployment perspective. We additionally note that less permanent building features, such as solar blinds, are likely to be a more near-term commercial opportunity than traditional windows. The opportunity to create rigid and bendable solar cells across all of the material classes discussed here, provides the necessary flexibility in terms of their mechanical properties for such applications.

From an aesthetic perspective, the colour and device structures need to be carefully considered. Because of the non-constant absorption coefficient of absorbing layers and the multi-layered structure of solar cells, transmission through a device will modify the colour coordinates of incident light, and do so with a changing degree as a function of absorber layer thickness [48]. This is conventionally counteracted through the introduction of passive, light-absorbing components (typically organic pigments) into the structure, at the cost of a reduced efficiency for a given transmittance [197]. Developing absorber materials or device structures that provide colour selectivity, whilst maximising efficiency remains a challenge. Arguably, organic device architectures possess the most flexibility in this regard due to their Gaussian absorption bands [261]. Through the development of novel pigments and polymers that maintain transparency in the visible, but can extend into the infrared, remains an opportunity in this space. In fact, simulations around such systems (see figure 15) indicate that efficiencies of up to 10% could be achieved for idealized organic systems with negligible absorption within the active layer across the visible [258].

Finally, from a processing perspective, scalability of technologies is paramount. As a practical example, the promising efficiencies of dye-sensitized solar cells on small-scale devices have not been translated to commercial scales. In contrast, the scalability of organic and inorganic devices have been demonstrated [4, 262]. One of the advantages of such ‘thin film’ structures is that they have been able to leverage from decades of knowledge garnered in the production of semi-transparent, amorphous silicon devices to accelerate their development into actual real-world technologies.

In conclusion, the development of high-efficiency semi-transparent solar cells provides an opportunity for solar cell disruption through its adoption as window- or roofing- based BIPV. This exciting area presents a lower barrier for entry for emerging photovoltaic technologies compared to rooftop markets because (i) unlikely crystalline silicon, they can be made inherently semi-transparent, and (ii) existing products exhibit relatively low efficiencies compared to what emerging technologies demonstrate already. Existing challenges around stability and toxicity are now key priority areas for research in this areas. Through a continuing focus on materials, device structures and their building integration, these challenges will be addressed, upon which time a new paradigm of high-efficiency, semi-transparent building integrated photovoltaic products will emerge.

Acknowledgments

JS acknowledges funding support through the Monash Graduate Scholarship and Monash International Postgraduate Research Scholarship programs. JJ acknowledges funding support through the Monash University Materials Science, Engineering Department and Faculty of Engineering new academic funding program and the Australian Research Council through CE170100026.

References

[1] Lewis N S 2016 Aspects of science and technology in support of legal and policy frameworks associated with a global carbon emissions-control regime *Energy Environ. Sci.* **9** 2172–6
[2] IEA 2015 25 Energy Efficiency Policy Recommendations 2011 *International Energy Agency (IEA)* Available at: https://www.iea.org/publications/freepublications/publication/25recom_2011.pdf
[3] Ryberg M W, Owsianiak M, Laurent A and Hauschild M Z 2015 Power generation from chemically cleaned coals: do environmental benefits of firing cleaner coal outweigh environmental burden of cleaning? *Energy Environ. Sci.* **8** 2435–47
[4] Green M A 2016 Commercial progress and challenges for photovoltaics *Nat. Energy* **1** 15015
[5] Lewis N S and Nocera D G 2006 Powering the planet: Chemical challenges in solar energy utilization *Proc. Natl. Acad. Sci.* **103** 15729–35
[6] Fraunhofer ISE: Photovoltaics Report, updated: 6 June 2016
[7] BP 2016 Statistical Review of World Energy 2016 http://www.bp.com/statisticalreview
[8] Saga T 2010 Advances in crystalline silicon solar cell technology for industrial mass production *NPG Asia Mater.* **2** 96–102
[9] Christensen C M 1997 *The Innovator's Dilemma: When New Technologies Cause Great Firms to Fail* (Boston, MA: Harvard Business School Press)
[10] Wong P W, Shimoda Y, Nonaka M, Inoue M and Mizuno M 2008 Semi-transparent PV: thermal performance, power generation, daylight modelling and energy saving potential in a residential application *Renew. Energy* **33** 1024–36
[11] Li D H W, Lam T N T and Cheung K L 2009 Energy and cost studies of semi-transparent photovoltaic skylight *Energy Convers. Manag.* **50** 1981–90
[12] Miyazaki T, Akisawa A and Kashiwagi T 2005 Energy savings of office buildings by the use of semi-transparent solar cells for windows *Renew. Energy* **30** 281–304
[13] López C S P and Sangiorgi M 2014 Comparison assessment of BIPV façade semi-transparent modules: further insights on human comfort conditions *Energy Procedia* **48** 1419–28
[14] Yoon J H, Song J and Lee S J 2011 Practical application of building integrated photovoltaic (BIPV) system using transparent amorphous silicon thin-film PV module *Sol. Energy* **85** 723–33
[15] Debije M 2015 Renewable energy: better luminescent solar panels in prospect *Nature* **519** 298–9
[16] Heinstein P, Ballif C and Perret-Aebi L E 2013 Building integrated photovoltaics (BIPV): review, potentials, barriers and myths *Green* **3** 125–56
[17] James T, Goodrich A, Woodhouse M, Margolis R and Ong S 2011 Building-integrated photovoltaics (BIPV) in the residential sector: an analysis of installed rooftop system prices *NREL Technical Report* NREL/TP-6A20-53103 US Department of Energy
[18] Pacheco-Torgal F 2014 Eco-efficient construction and building materials research under the EU framework programme horizon 2020 *Constr. Build. Mater.* **51** 151–62
[19] Bonomo P, Chatzipanagi A and Frontini F 2015 Overview and analysis of current BIPV products: new criteria for supporting the technological transfer in the building sector *Vitruvio* **1** 67–85
[20] n-tech Research 2014 *BIPV Glass Markets-2014 and Beyond* Report #Nano-707
[21] Prasad D and Snow M 2005 *Designing with Solar Power: a Source Book for Building Integrated Photovoltaics (BIPV)* (Mulgrave, Australia: Images Publishing)
[22] Norton B, Eames P C, Mallick T K, Huang M J, McCormack S J, Mondol J D and Yohanis Y G 2011 Enhancing the performance of building integrated photovoltaics *Sol. Energy* **85** 1629–64
[23] Verberne G, Bonomo P, Frontini F, van den Donker M N, Chatzipanagi A, Sinapis K and Folkerts W 2015 BIPV product overview for solar façades and roofs *SUPSI-SEAC*
[24] Jelle B P, Breivik C and Drolsum Røkenes H 2012 Building integrated photovoltaic products: a state-of-the-art review and future research opportunities *Sol. Energy Mater. Sol. Cells* **100** 69–96
[25] Chopra K L, Paulson P D and Dutta V 2004 Thin-film solar cells: an overview *Prog. Photovolt: Res. Appl.* **12** 69–92
[26] Tang C W 1986 Two-layer organic photovoltaic cell *Appl. Phys. Lett.* **48** 183–5
[27] Yu G, Gao J, Hummelen J C, Wudl F and Heeger A J 1995 Polymer photovoltaic cells—enhanced efficiencies via a network of internal donor-acceptor heterojunctions *Science* **270** 1789–91
[28] Halls J J M, Walsh C A, Greenham N C, Marseglia E A, Friend R H, Moratti S C and Holmes A B 1995 Efficient photodiodes from interpendetrating polymer networks *Nature* **376** 498–500
[29] O'Regan B and Grätzel M 1991 A low-cost, high-efficiency solar cell based on dye-sensitized colloidal TiO_2 films *Nature* **353** 737–40
[30] Lee M M, Teuscher J, Miyasaka T, Murakami T N and Snaith H J 2012 Efficient hybrid solar cells based on meso-superstructured organometal halide perovskites *Science* **338** 643–7
[31] Green M A, Emery K, Hishikawa Y, Wilhelm W and Dunlop E D 2016 Solar cell efficiency tables (version 48) *Prog. Photovolt: Res. Appl.* **24** 905–13
[32] Biancardo M, Taira K, Kogo N, Kikuchi H, Kumagai N, Kuratani N, Inagawa I, Imoto S and Nakata J 2007 Characterization of microspherical semi-transparent solar cells and modules *Sol. Energy* **81** 711–6
[33] Gueymard C A, Myers D and Emery K 2002 Proposed reference irradiance spectra for solar energy systems testing *Sol. Energy* **73** 443–67
[34] Li D H W, Lam T N T, Cheung K L and Tang H L 2008 An analysis of luminous efficacies under the CIE standard skies *Renew. Energy* **33** 2357–65
[35] Li D H W 2007 Daylight and energy implications for CIE standard skies *Energy Convers. Manag.* **48** 745–55
[36] Martínez-Rubio A, Sanz-Adan F, Santamaría-Peña J and Martínez A 2016 Evaluating solar irradiance over facades in high building cities, based on LiDAR technology *Appl. Energy* **183** 133–47
[37] Li D H W, Lam T N T, Chan W W H and Mak A H L 2009 Energy and cost analysis of semi-transparent photovoltaic in office buildings *Appl. Energy* **86** 722–9
[38] Clarke J A, Hand J W, Johnstone C M, Kelly N and Strachan P A 1996 Photovoltaic-integrated building facades *Renew. Energy* **8** 475–9

[39] Chow T T, Qiu Z and Li C 2009 Potential application of 'see-through' solar cells in ventilated glazing in Hong Kong *Sol. Energy Mater. Sol. Cells* **93** 230–8

[40] Sullivan R, Lee E S and Selkowitz S 1992 A method of optimizing solar control and daylighting performance in commercial buildings *AHRAE/DOE/BTECC Conf. Proc. in Thermal Performance of the Exterior Envelopes of Buildings V* LBL-32931 (Lawrence Berkeley Laboratory, CA)

[41] Australian Building Council Board (ABCB) 2016 *National Construction Code: Energy Efficiency Provisions* Section J6: Artificial Lighting and Power

[42] Bodart M A and De Harde A 2002 Global energy savings in offices by the use of daylight *Energy Build.* **34** 421–9

[43] Chehab O 1994 Intelligent facade: photovoltaic and architecture *Renew. Energy* **5** 188–204

[44] Grätzel M 2003 *J. Photochem. Photobiol.* A **4** 145–53

[45] Baetens R, Jelle B P and Gustavsen A 2010 Properties, requirements and possibilities of smart windows for dynamic daylight and solar energy control in buildings: a state-of-the-art review *Sol. Energy Mater. Sol. Cells* **94** 87–105

[46] Granqvist C G 1993 Transparent conductive electrodes for electrochromic devices: a review *Appl. Phys.* A **57** 19–24

[47] Facchetti A and Marks T J 2010 *Transparent Electronics: from Synthesis to Applications* (Chichester: Wiley)

[48] Della Gaspera E, Peng Y, Hou Q, Spiccia L, Bach U, Jasieniak J J and Cheng Y B 2015 Ultra-thin high efficiency semitransparent perovskite solar cells *Nano Energy* **13** 249–57

[49] Ellmer K 2012 Past achievements and future challenges in the development of optically transparent electrodes *Nat. Photon.* **6** 808–16

[50] Ye S, Rathmell A R, Chen Z, Stewart I E and Wiley B J 2014 Metal nanowire networks: the next generation of transparent conductors *Adv. Mater.* **26** 6670–87

[51] Po R, Carbonera C, Bernardi A, Tinti F and Camaioni N 2012 Polymer- and carbon-based electrodes for polymer solar cells: toward low-cost, continuous fabrication over large area *Sol. Energy Mater. Sol. Cells* **100** 97–114

[52] Selvaraju T and Ramaraj R 2005 Electrochemically deposited nanostructured platinum on Nafion coated electrode for sensor applications *J. Electroanal. Chem.* **585** 290–300

[53] Brabec C J, Cravino A, Meissner D, Sariciftci N S, Thomas F, Rispens M T, Sanchez L and Hummelen J C 2001 Origin of the open circuit voltage of plastic solar cells *Adv. Funct. Mater.* **11** 374–80

[54] Minami T 2005 Transparent conducting oxide semiconductors for transparent electrodes *Semicond. Sci. Technol.* **20** S35–44

[55] Chittik R C, Alexander J H and Sterling H F 1969 The preparation and properties of amorphous silicon *J. Electrochem. Soc.* **116** 77–81

[56] Shah A V, Schade H, Vanecek M, Meier J, Vallat-Sauvain E, Wyrsch N, Kroll U, Droz C and Bailat J 2004 Thin-film silicon solar cell technology *Prog. Photovolt: Res. Appl.* **12** 113–42

[57] Hamakawa Y and Okamoto H 1989 Amorphous silicon solar cells *Adv. Sol. Energy* **5** 1–98

[58] Staebler D L and Wronski C R 1977 Reversible conductivity changes in discharge-produced amorphous Si *Appl. Phys. Lett.* **31** 292–4

[59] Green M A 2007 Thin-film solar cells: review of materials, technologies and commercial status *J. Mater. Sci., Mater. Electron.* **18** 15–9

[60] Takeoka A *et al* 1993 Development and application of see-through a-Si solar cells *Sol. Energy Mater. Sol. Cells* **29** 243–52

[61] Kishi Y, Inoue H and Tanaka H 1989 Photovoltaic device *US Patent Specification* US 4795500 A

[62] Hamakawa Y 1985 Recent progress of amorphous silicon solar cell technology *Mater. Res. Soc.* **49** 239–50

[63] You D J, Kim S H, Lee H, Chung J-W, Hwang S-T, Heo Y H, Lee S and Lee H-M 2015 Recent progress of high efficiency Si thin-film solar cells in large area *Prog. Photovolt: Res. Appl.* **23** 973–88

[64] Schropp R E I, Adachi K, Imajyo N, Del Cueto J A, Bhat P K and Madan A 1989 Semi-transparent amorphous silicon solar cells *Mater. Res. Soc.* **149** 429–34

[65] Wook L J, Shin M, Lee D J, Hyun L S and Jin Y S 2014 Highly transparent amorphous silicon solar cells fabricated using thin absorber and high-bandgap-energy *n*/*i*-interface layers *Sol. Energy Mater. Sol. Cells* **128** 301–6

[66] Lim J W, Lee S H, Lee D J, Lee Y J and Yun S J 2013 Performances of amorphous silicon and silicon germanium semi-transparent solar cells *Thin Solid Films* **547** 212–5

[67] Chevallier J, Wieder H, Onton A and Guarnieri C R 1977 Optical properties of amorphous $SixGe_{1-x}$(H) alloys prepared by R F glow discharge *Solid State Commun.* **24** 867–9

[68] Bullot J and Schmidt M P 1987 Physics of amorphous silicon–carbon alloys *Phys. Status Solidi* b **143** 345–418

[69] Bullock J N, Bechinger C, Benson D K and Branz H M 1996 Semi-transparent *a*-SiC:H solar cells for self-powered photovoltaic-electrochromic devices *J. Non-Cryst. Solids* **198–200** 1163–7

[70] Gao W, Lee S, Bullock J, Xu Y, Benson D, Morrison S and Branz H 1999 First *a*-SiC:H photovoltaic-powered monolithic tandem electrochromic smart window device *Sol. Energy Mater. Sol. Cells* **59** 243–54

[71] Hanaki K, Hattori Y, Nakabayashi H, Yamaguchi S and Hamakawa Y 1989 A semi-transparent solar cell using *a*-SiC *Mater. Res. Soc.* **149** 395–404

[72] Shay J L, Wagner S and Kasper H M 1975 Efficient $CuInSe_2$/CdS solar cells *Appl. Phys. Lett.* **27** 89–90

[73] Gabor A M, Tuttle J R, Albin D S, Contreras M A, Noufi R and Hermann A M 1994 High-efficiency $CuIn_xGa_{1-x}Se_2$ solar cells made from $(In_x,Ga_{1-x})_2Se_3$ precursor films *Appl. Phys. Lett.* **65** 198–200

[74] Contreras M A, Egaas B, Ramanathan K, Hiltner J, Swartzlander A, Hasoon F and Noufi R 1999 Progress toward 20% efficiency in $Cu(In,Ga)Se_2$ polycrystalline thin-film solar cells *Prog. Photovolt: Res. Appl.* **7** 311–6

[75] Chirilă A *et al* 2013 Potassium-induced surface modification of $Cu(In,Ga)Se_2$ thin films for high-efficiency solar cells *Nat. Mater.* **12** 1107–11

[76] Delahoy A E, Chen L, Akhtar M, Sang B and Guo S 2004 New technologies for CIGS photovoltaics *Sol. Energy* **77** 785–93

[77] Nakada T, Hirabayashi Y and Tokado T 2002 $Cu(In_{1-x},Ga_x)Se_2$-based thin film solar cells using transparent conducting back contacts *Japan. J. Appl. Phys.* **41** L1209–11

[78] Nakada T, Hirabayashi Y, Tokado T, Ohmori D and Mise T 2004 Novel device structure for $Cu(In,Ga)Se_2$ thin film solar cells using transparent conducting oxide back and front contacts *Sol. Energy* **77** 739–47

[79] Young D L, Abushama J, Noufi R, Li X, Keane J, Gessert T A, Ward J S, Contreras M and Coutts T J 2002 A new thin-film $CuGaSe_2$/$Cu(In,Ga)Se_2$ bifacial, tandem solar cell with both junctions formed simultaneously *29th IEEE Photovoltaic Specialists Conf.* 608–11

[80] Morgan D V, Aliyu Y H, Bunce R W and Salehi A 1998 Annealing effects on opto-electronic properties of sputtered and thermally evaporated indium-tin-oxide films *Thin Solid Films* **312** 268–72

[81] Jiang X, Wong F L, Fung M K and Lee S T 2003 Aluminum-doped zinc oxide films as transparent conductive electrode for organic light-emitting devices *Appl. Phys. Lett.* **83** 1875–7

[82] Chirilă A *et al* 2011 Highly efficient Cu(In,Ga)Se_2 solar cells grown on flexible polymer films *Nat. Mater.* **10** 857–61

[83] Nishiwaki S, Siebentritt S, Walk P and Lux-Steiner M C 2003 A stacked chalcopyrite thin-film tandem solar cell with 1.2 V open-circuit voltage *Prog. Photovolt: Res. Appl.* **11** 243–8

[84] Shafarman W N, Birkmire R W, Marsillac S, Marudachalam M, Orbey N and Russell T W F 1997 Effect of reduced deposition temperature, time, and thickness on Cu(InGa)Se_2 films and devices *26th IEEE Photovoltaic Specialists Conf.* 1–4

[85] Ramanathan K, Noufi R, To B, Young D L, Bhattacharya R, Contreras M A, Dhere R G and Teeter G 2007 Processing and properties of sub-micron CIGS solar cells *2006 IEEE 4th World Conf. Photovolt. Energy Conversion, WCPEC-4* **1** 380–3

[86] Lundberg O, Bodegard M, Malmstrom J and Stolt L 2003 Influence of the Cu(In,Ga)Se_2 thickness and Ga grading on solar cell performance *Prog. Photovolt: Res. Appl.* **11** 77–88

[87] Saifullah M *et al* 2016 Development of Semitransparent CIGS thin-film solar cells modified with a sulfurized-AgGa layer for building applications *J. Mater. Chem.* A **4** 10542–51

[88] McLeod S M, Hages C J, Carter N J and Agrawal R 2015 Synthesis and characterization of 15% efficient CIGSSe solar cells from nanoparticle inks *Prog. Photovolt: Res. Appl.* **23** 1550–6

[89] Todorov T K, Gunawan O, Gokmen T and Mitzi D B 2013 Solution-processed Cu(In,Ga)$(S,Se)_2$ absorber yielding a 15.2% efficient solar cell *Prog. Photovolt: Res. Appl.* **21** 82–7

[90] Chu V B, Park S J, Park G S, Jeon H S, Hwang Y J and Min B K 2016 Semi-transparent thin film solar cells by a solution process *Korean J. Chem. Eng.* **33** 880–4

[91] Moon S H, Park S J, Hwang Y J, Lee D K, Cho Y, Kim D W and Min B K 2014 Printable, wide band-gap chalcopyrite thin films for power generating window applications *Sci. Rep.* **4** 4408

[92] Ito K 2015 *Copper Zinc Tin Sulfide-Based Thin-Film Solar Cells* (Chichester: Wiley)

[93] Nitsche R, Sargent D F and Wild P 1967 Crystal growth of quaternary 1_2246_4 chalcogenides by iodine vapor transport *J. Cryst. Growth* **1** 52–3

[94] Ito K and Nakazawa T 1988 Electrical and optical properties of stannite-type quarternary semiconductor thin films *Japan. J. Appl. Phys.* **27** 2094–7

[95] Barkhouse D A R, Gunawan O, Gokmen T, Todorov T K and Mitzi D B 2012 Device characteristics of a 10.1% hydrazine-processed CZTSSe solar cell *Prog. Photovolt: Res. Appl.* **20** 6–11

[96] Ki W and Hillhouse H W 2011 Earth-abundant element photovoltaics directly from soluble precursors with high yield using a non-toxic solvent *Adv. Energy Mater.* **1** 732–5

[97] Guo Q, Ford G M, Yang W, Walker B C, Stach E A, Hillhouse H W and Agrawal R 2010 Fabrication of 7.2% Efficient CZTSSe solar cells using CZTS nanocrystals *J. Am. Chem. Soc.* **132** 17384–6

[98] Embden J V, Chesman A S R, Gaspera E D, Du N W, Watkins S E and Jasieniak J J 2014 $Cu_2ZnSnS_{4x}Se_{4(1-x)}$ solar cells from polar nanocrystal inks *J. Am. Chem. Soc* **4** 5237–40

[99] Sarswat P K and Free M L 2011 Demonstration of a sol-gel synthesized bifacial CZTS photoelectrochemical cell *Phys. Status Solidi* a **208** 2861–4

[100] Sarswat P K, Snure M, Free M L and Tiwari A 2012 CZTS thin films on transparent conducting electrodes by electrochemical technique *Thin Solid Films* **520** 1694–7

[101] Ge J, Chu J, Jiang J, Yan Y and Yang P 2014 Characteristics of in-substituted CZTS thin film and bifacial solar cell *ACS Appl. Mater. Interfaces* **6** 21118–30

[102] Ge J, Chu J, Jiang J, Yan Y and Yang P 2015 The interfacial reaction at ITO back contact in kesterite CZTSSe bifacial solar cells *ACS Sustain. Chem. Eng.* **3** 3043–52

[103] Ge J, Yu Y, Ke W, Li J, Tan X, Wang Z, Chu J and Yan Y 2016 Improved performance of electroplated CZTS thin-film solar cells with bifacial configuration *ChemSusChem* **9** 2149–58

[104] Kim J *et al* 2014 2014 High efficiency $Cu_2ZnSn(S,Se)_4$ solar cells by applying a double In_2S_3/CdS emitter *Adv. Mater.* **26** 7427–31

[105] Kuo D H and Tsega M 2014 Electrical conduction and mobility enhancement in *p*-type In-doped $Cu_2ZnSnSe_4$ bulks *Japan. J. Appl. Phys.* **53** 35801

[106] Frerichs R 1947 The photo-conductivity of 'incomplete phosphors' *Phys. Rev.* **72** 594–601

[107] Loferski J J 1956 Theoretical considerations governing the choice of the optimum semiconductor for photovoltaic solar energy conversion *J. Appl. Phys.* **27** 777–84

[108] McCandless B E and Sites J R 2011 Cadmium Telluride Solar Cells *Handbook of Photovoltaic Science and Engineering* 2nd edn (Chichester: Wiley)

[109] Morales-Acevedo A 2006 Thin film CdS/CdTe solar cells: research perspectives *Sol. Energy* **80** 675–81

[110] Williams B L, Major J D, Bowen L, Phillips L, Zoppi G, Forbes I and Durose K 2014 Challenges and prospects for developing CdS/CdTe substrate solar cells on Mo foils *Sol. Energy Mater. Sol. Cells* **124** 31–8

[111] Dhere R G, Duenow J N, Dehart C M, Li J V, Kuciauskas D and Gessert T A 2012 Development of substrate structure CdTe photovoltaic devices with performance exceeding 10% *38th IEEE Photovoltaic Specialists Conf.* 3208–11

[112] Romeo A, Terheggen M, Abou-Ras D, Bätzner D L, Haug F-J, Kälin M, Rudmann D and Tiwari A N 2004 Development of thin-film Cu(In,Ga)Se_2 and CdTe solar cells *Prog. Photovolt: Res. Appl.* **12** 93–111

[113] Birkmire R W, Mccandless B E and Shafarman W N 1988 CdTe/CdS solar cells with transparent contacts *Sol. Cells* **23** 115–26

[114] Tiwari A N, Khrypunov G, Kurdzesau F, Bätzner D L, Romeo A and Zogg H 2004 CdTe solar cell in a novel configuration *Prog. Photovolt: Res. Appl.* **12** 33–8

[115] Romeo A, Khrypunov G, Galassini S, Zogg H and Tiwari A N 2007 Bifacial configurations for CdTe solar cells *Sol. Energy Mater. Sol. Cells* **91** 1388–91

[116] Meyers P V, Liu C H, Russell L, Ramanathan V, Birkmire R W, McCandless B E and Phillips J E 1988 Polycrystalline CdTe on $CuInSe_2$ cascade solar cells *20th IEEE Photovoltaic Specialists Conf.* 1448–51

[117] Mondal A, McCandless B E and Birkmire R W 1992 Electrochemical deposition of thin ZnTe films as a contact for CdTe solar cells *Sol. Energy Mater. Sol. Cells* **26** 181–7

[118] Desai D, Hegedus S, McCandless B and Ryan D 2005 Transparent ZnTe:Cu contacts for bifacial characterization of CdTe solar cells *Mater. Res. Soc.* **865** 405–10

[119] Wu X, Zhou J, Duda A, Keane J C, Gessert T A, Yan Y and Noufi R 2006 13.9%-efficient CdTe polycrystalline thin-film solar cells with an infrared transmission of ~50% *Prog. Photovolt: Res. Appl.* **14** 471–83

[120] Barnes T M, Wu X, Zhou J, Duda A, Van De Lagemaat J, Coutts T J, Weeks C L, Britz D A and Glatkowski P 2007 Single-wall carbon nanotube networks as a transparent back contact in CdTe solar cells *Appl. Phys. Lett.* **90** 243503

[121] Kosyachenko L A, Mathew X, Roshko V Y and Grushko E V 2013 Optical absorptivity and recombination losses: the limitations imposed by the thickness of absorber layer in CdS/CdTe solar cells *Sol. Energy Mater. Sol. Cells* **114** 179–85

[122] Paudel N R, Wieland K A and Compaan A D 2012 Ultrathin CdS/CdTe solar cells by sputtering *Sol. Energy Mater. Sol. Cells* **105** 109–12

[123] Jasieniak J, Macdonald B I, Watkins S E and Mulvaney P 2011 Solution- processed sintered nanocrystal solar cells via layer-by-layer assembly *Nano Lett.* **11** 2856–64

[124] Burkhard G F, Hoke E T and McGehee M D 2010 Accounting for interference, scattering, and electrode absorption to make accurate internal quantum efficiency measurements in organic and other thin solar cells *Adv. Mater.* **22** 3293–7

[125] Marsillac S, Parikh V Y and Compaan A D 2007 Ultra-thin bifacial CdTe solar cell *Sol. Energy Mater. Sol. Cells* **91** 1398–402

[126] Heisler C, Schnohr C S, Hädrich M, Oertel M, Kraft C, Reislöhner U, Metzner H and Wesch W 2013 Transparent CdTe solar cells with a ZnO:Al back contact *Thin Solid Films* **548** 627–31

[127] Plotnikov V V, Carter C W, Stayancho J M, Paudel N R, Mahabaduge H, Kwon D, Grice C R and Compaan A D 2013 Semitransparent PV windows with sputtered CdS/CdTe thin films *39th IEEE Photovoltaic Specialists Conf.* 405–8

[128] Gupta A and Compaan A D 2004 All-sputtered 14% CdS/CdTe thin-film solar cell with ZnO: Al transparent conducting oxide *Appl. Phys. Lett.* **85** 684–6

[129] Jones E W, Barrioz V, Irvine S J C and Lamb D 2009 Towards ultra-thin CdTe solar cells using MOCVD *Thin Solid Films* **517** 2226–30

[130] MacDonald B I, Della Gaspera E, Watkins S E, Mulvaney P and Jasieniak J J 2014 Enhanced photovoltaic performance of nanocrystalline CdTe/ZnO solar cells using sol-gel ZnO and positive bias treatment *J. Appl. Phys.* **115** 184501

[131] Mccandless B E and Buchanan W A 2008 High throughput processing of CdTe/CdS solar cells with thin absorber layers *33rd IEEE Photovoltaic Specialists Conf.* 1–6

[132] Panthani M G, Kurley J M, Crisp R W, Dietz T C, Ezzyat T, Luther J M and Talapin D V 2014 High efficiency solution processed sintered CdTe nanocrystal solar cells: the role of interfaces *Nano Lett.* **14** 670–5

[133] Plotnikov V V, Kwon D, Wieland K A and Compaan A D 2009 10% Efficiency solar cells with 0.5 μm of CdTe *34th IEEE Photovoltaic Specialists Conf.* 1435–8

[134] So S, Hwang I and Schmuki P 2015 Hierarchical DSSC structures based on 'single walled' TiO_2 nanotube arrays reach a back-side illumination solar light conversion efficiency of 8% *Energy Environ. Sci.* **8** 849–54

[135] Hu Y H 2014 Novel meso-superstructured solar cells with a high efficiency exceeding 12% *Adv. Mater.* **26** 2102–4

[136] Yella A, Lee H-W, Tsao H N, Yi C, Chandiran A K, Nazeeruddin M K, Diau E W-G, Yeh C-Y, Zakeeruddin S M and Grätzel M 2011 Porphyrin-sensitized solar cells with cobalt (II/III)-based redox electrolyte exceed 12% efficiency *Science* **334** 629–34

[137] Mathew S, Yella A, Gao P, Humphry-Baker R, Curchod B F E, Ashari-Astani N, Tavernelli I, Rothlisberger U, Nazeeruddin M K and Grätzel M 2014 Dye-sensitized solar cells with 13% efficiency achieved through the molecular engineering of porphyrin sensitizers *Nat. Chem.* **6** 242–7

[138] Kakiage K, Aoyama Y, Yano T, Oya K, Fujisawa J and Hanaya M 2015 Highly-efficient dye-sensitized solar cells with collaborative sensitization by silyl-anchor and carboxy-anchor dyes *Chem. Commun.* **51** 15894–7

[139] Hardin B E, Snaith H J and Mcgehee M D 2012 The renaissance of dye-sensitized solar cells *Nat. Photon.* **6** 162–9

[140] Al-Alwani M A M, Mohamad A B, Ludin N A, Kadhum A A H and Sopian K 2016 Dye-sensitised solar cells: development, structure, operation principles, electron kinetics, characterisation, synthesis materials and natural photosensitisers *Renew. Sustain. Energy Rev.* **65** 183–213

[141] Odobel F, Le Pleux L, Pellegrin Y and Blart E 2010 New photovoltaic devices based on the sensitization of *p*-type semiconductors: challenges and opportunities *Acc. Chem. Res.* **43** 1063–71

[142] Yoon S, Tak S, Kim J, Jun Y, Kang K and Park J 2011 Application of transparent dye-sensitized solar cells to building integrated photovoltaic systems *Build. Environ.* **46** 1899–904

[143] Ito S, Chen P, Comte P, Nazeeruddin M K, Liska P, Pechy P and Grätzel M 2007 Fabrication of screen-printing pastes from TiO_2 powders for dye-sensitised solar cells *Prog. Photovolt: Res. Appl.* **15** 603–12

[144] Barbé C J, Arendse F, Comte P, Jirousek M, Lenzmann F, Shklover V, Gra M and Grätzel M 1997 Nanocrystalline titanium oxide electrodes for photovoltaic applications *J. Am. Ceram. Soc.* **80** 3157–71

[145] Chen D, Huang F, Cheng Y B and Caruso R A 2009 Mesoporous anatase TiO_2 beads with high surface areas and controllable pore sizes: a superior candidate for high-performance dye-sensitized solar cells *Adv. Mater.* **21** 2206–10

[146] Gong J, Liang J and Sumathy K 2012 Review on dye-sensitized solar cells (DSSCs): fundamental concepts and novel materials *Renew. Sustain. Energy Rev.* **16** 5848–60

[147] Hamann T W, Jensen R A, Martinson A B F, Van Ryswyk H and Hupp J T 2008 Advancing beyond current generation dye-sensitized solar cells *Energy Environ. Sci.* **1** 66–78

[148] Li B, Wang L, Kang B, Wang P and Qiu Y 2006 Review of recent progress in solid-state dye-sensitized solar cells *Sol. Energy Mater. Sol. Cells* **90** 549–73

[149] Yum J, Chen P, Grätzel M and Nazeeruddin M K 2008 Recent developments in solid-state dye-sensitized solar cells *ChemSusChem* **1** 699–707

[150] Zheng Y Z, Tao X, Hou Q, Wang D T, Zhou W L and Chen J F 2011 Iodine-doped ZnO nanocrystalline aggregates for improved dye-sensitized solar cells *Chem. Mater.* **23** 3–5

[151] Ko K H, Lee Y C and Jung Y J 2005 Enhanced efficiency of dye-sensitized TiO_2 solar cells (DSSC) by doping of metal ions *J. Colloid Interface Sci.* **283** 482–7

[152] Wang P, Zakeeruddin S M, Humphry-Baker R, Moser J E and Grätzel M 2003 Molecular-scale interface engineering of TiO_2 nanocrystals: improving the efficiency and stability of dye-sensitized solar cells *Adv. Mater.* **15** 2101–4

[153] Wang P, Zakeeruddin S M, Comte P, Charvet R, Humphry-baker R and Grätzel M 2003 Enhance the performance of dye-sensitized solar cells by co-grafting amphiphilic sensitizer and hexadecylmalonic acid on TiO_2 nanocrystals *Phys. Chem.* **107** 14336–41

[154] Wang Z S, Huang C H, Huang Y Y, Hou Y J, Xie P H, Zhang B W and Cheng H M 2001 A highly efficient solar cell made from a dye-modified ZnO-covered TiO_2 nanoporous electrode *Chem. Mater.* **13** 678–82

[155] Kim J and Kim J 2011 Fabrication of dye-sensitized solar cells using Nb_2O_5 blocking layer made by sol-gel method *J. Nanosci. Nanotechnol.* **11** 7335–8

[156] Gonçalves L M, de Zea Bermudez V, Ribeiro H A and Mendes A M 2008 Dye-sensitized solar cells: a safe bet for the future *Energy Environ. Sci.* **1** 655–67

[157] Calogero G, Calandra P, Irrera A, Sinopoli A, Citro I and Di Marco G 2011 A new type of transparent and low cost counter-electrode based on platinum nanoparticles for dye-sensitized solar cells *Energy Environ. Sci.* **4** 1838–44
[158] Olsen E, Hagen G and Lindquist S E 2000 Dissolution of platinum in methoxy propionitrile containing LiI/I_2 *Sol. Energy Mater. Sol. Cells* **63** 267–73
[159] Theerthagiri J, Senthil A R, Madhavan J and Maiyalagan T 2015 Recent Progress in non-platinum counter electrode materials for dye-sensitized solar cells *ChemElectroChem* **2** 928–45
[160] Chen P Y, Li C T, Lee C P, Vittal R and Ho K C 2015 PEDOT-decorated nitrogen-doped graphene as the transparent composite film for the counter electrode of a dye-sensitized solar cell *Nano Energy* **12** 374–85
[161] Ameen S, Shaheer Akhtar M, Kim Y S, Yang O B and Shin H S 2010 Sulfamic acid-doped polyaniline nanofibers thin film-based counter electrode: application in dye-sensitized solar cells *J. Phys. Chem.* C **114** 4760–4
[162] Tai Q, Chen B, Guo F, Xu S, Hu H, Sebo B and Zhao X Z 2011 *In situ* prepared transparent polyaniline electrode and its application in bifacial dye-sensitized solar cells *ACS Nano* **5** 3795–9
[163] Wu J, Li Y, Tang Q, Yue G, Lin J, Huang M and Meng L 2014 Bifacial dye-sensitized solar cells: a strategy to enhance overall efficiency based on transparent polyaniline electrode *Sci. Rep.* **4** 4028
[164] Wei W, Wang H and Hu Y H 2014 A review on PEDOT-based counter electrodes for dye-sensitized solar cells *Int. J. Energy Res.* **38** 1099–111
[165] Wang H and Hu Y H 2012 Graphene as a counter electrode material for dye-sensitized solar cells *Energy Environ. Sci.* **5** 8182–8
[166] Zhang D W, Li X D, Li H B, Chen S, Sun Z, Yin X J and Huang S M 2011 Graphene-based counter electrode for dye-sensitized solar cells *Carbon N. Y.* **49** 5382–8
[167] Roy-Mayhew J D, Bozym D J, Punckt C and Aksay I A 2010 Functionalized graphene as a catalytic counter electrode in dye-sensitized solar cells *ACS Nano* **4** 6203–11
[168] Wang M, Anghel A M, Marsan B, Ha N C, Pootrakulchote N, Nazeeruddin M K and Grätzel M 2009 CoS Supersedes Pt as efficient electrocatalyst for triiodide reduction in dye-sensitized solar cells *J. Am. Chem. Soc.* **131** 15976–7
[169] Gao J, Yang Y, Zhang Z, Yan J, Lin Z and Guo X 2016 Bifacial quasi-solid-state dye-sensitized solar cells with poly (vinyl pyrrolidone)/polyaniline transparent counter electrode *Nano Energy* **26** 123–30
[170] Biancardo M, West K and Krebs F C 2006 Optimizations of large area quasi-solid-state dye-sensitized solar cells *Sol. Energy Mater. Sol. Cells* **90** 2575–88
[171] Kawano R, Matsui H, Matsuyama C, Sato A, Susan M A B H, Tanabe N and Watanabe M 2004 High performance dye-sensitized solar cells using ionic liquids as their electrolytes *J. Photochem. Photobiol.* A **164** 87–92
[172] Li D, Qin D, Deng M, Luo Y and Meng Q 2009 Optimization the solid-state electrolytes for dye-sensitized solar cells *Energy Environ. Sci.* **2** 283–91
[173] Bach U, Lupo D, Comte P, Moser J, Weissörtel F, Salbeck J, Spreitzer H and Grätzel M 1998 Solid-state dye-sensitized mesoporous TiO_2 solar cells with high photon-to-electon conversion efficiencies *Nature* **395** 583–5
[174] Chung I, Lee B, He J, Chang R P H and Kanatzidis M G 2012 All-solid-state dye-sensitized solar cells with high efficiency *Nature* **485** 486–9
[175] Liu X, Zhang W, Uchida S, Cai L, Liu B and Ramakrishna S 2010 An efficient organic-dye-sensitized solar cell with *in situ* polymerized poly(3,4-ethylenedioxythiophene) as a hole-transporting material *Adv. Mater.* **22** 150–5
[176] Meng Q B, Takahashi K, Zhang X T, Sutanto I, Rao T N, Sato O, Fujishima A, Watanabe H, Nakamori T and Uragami M 2003 Fabrication of an efficient solid-state dye-sensitized solar cell *Langmuir* **19** 3572–4
[177] Boix P P, Larramona G, Jacob A, Delatouche B and Bisquert J 2012 Hole transport and recombination in all-solid Sb_2S_3-sensitized TiO_2 solar cells using CuSCN as hole transporter *J. Phys. Chem.* C **116** 1579–87
[178] Bandara J and Weerasinghe H 2005 Solid-state dye-sensitized solar cell with *p*-type NiO as a hole collector *Sol. Energy Mater. Sol. Cells* **85** 385–90
[179] Kolemen S, Cakmak Y, Erten-Ela S, Altay Y, Brendel J, Thelakkat M and Akkaya E U 2010 Solid-state dye-sensitized solar cells using red and near-IR absorbing bodipy sensitizers *Org. Lett.* **12** 3812–5
[180] Colonna D, Capogna V, Lembo A, Brown T M, Reale A and Di Carlo A 2012 Efficient cosensitization strategy for dye-sensitized solar cells *Appl. Phys. Express* **5** 2–5
[181] Joly D, Pelleja L, Narbey S, Oswald F, Meyer T, Kervella Y, Maldivi P, Clifford J N, Palomares E and Demadrille R 2015 Metal-free organic sensitizers with narrow absorption in the visible for solar cells exceeding 10% efficiency *Energy Environ. Sci.* **8** 2010–8
[182] Hara K *et al* 2005 Novel conjugated organic dyes for efficient dye-sensitized solar cells *Adv. Funct. Mater.* **15** 246–52
[183] Chiron J, Clifford J N, Joly D, Pelleja L, Palomares E and Demadrille R 2014 A Robust organic dye for dye sensitized solar cells based on iodine/iodide electrolytes combining high efficiency *Sci. Rep.* **4** 4033
[184] Reddy P Y *et al* 2007 Efficient sensitization of nanocrystalline TiO_2 films by a near-IR-absorbing unsymmetrical zinc phthalocyanine *Angew. Chem., Int. Ed.* **46** 373–6
[185] Matsui M, Hashimoto Y, Funabiki K, Jin J Y, Yoshida T and Minoura H 2005 Application of near-infrared absorbing heptamethine cyanine dyes as sensitizers for zinc oxide solar cell *Synth. Met.* **148** 147–53
[186] Yum J, Walter P, Huber S, Rentsch D, Geiger T, Nüesch F, De Angelis F, Grätzel M and Nazeeruddin M K 2007 Efficient far red sensitization of nanocrystalline TiO_2 films by an unsymmetrical squaraine dye *J. Am. Chem. Soc.* **129** 10320–1
[187] McMeekin D P *et al* 2016 A mixed-cation lead mixed-halide perovskite absorber for tandem solar cells *Science* **351** 151–5
[188] Yang Z, Rajagopal A, Chueh C C, Jo S B, Liu B, Zhao T and Jen A K Y 2016 Stable low-bandgap Pb–Sn binary perovskites for tandem solar cells *Adv. Mater.* **28** 8990–7
[189] Gao P, Grätzel M and Nazeeruddin M K 2014 Environmental science organohalide lead perovskites for photovoltaic applications *Energy Environ. Sci.* **1** 2448–63
[190] Salau A M 1980 Fundamental absorption edge in PbI_2:KI alloys *Sol. Energy Mater.* **2** 327–32
[191] Green M A, Ho-Baillie A and Snaith H J 2014 The emergence of perovskite solar cells *Nat. Photon.* **8** 506–14
[192] Song T B, Chen Q, Zhou H, Jiang C, Wang H H, Yang Y, Liu Y, You J and Yang Y 2015 Perovskite solar cells: film formation and properties *J. Mater. Chem.* A **3** 9032–50
[193] Park N G 2015 Perovskite solar cells: an emerging photovoltaic technology *Mater. Today* **18** 65–72

[194] Kang R, Yeo J S, Lee H J, Lee S, Kang M, Myoung N, Yim S Y, Oh S H and Kim D Y 2016 Exploration of fabrication methods for planar $CH_3NH_3PbI_3$ perovskite solar cells *Nano Energy* **27** 175–84

[195] Kojima A, Teshima K, Shirai Y and Miyasaka T 2009 Organometal halide perovskites as visible-light sensitizers for photovoltaic cells *J. Am. Chem. Soc.* **131** 6050–1

[196] Kim H S *et al* 2012 Lead iodide perovskite sensitized all-solid-state submicron thin film mesoscopic solar cell with efficiency exceeding 9% *Sci. Rep.* **2** 591

[197] Ramírez Quiroz C O, Bronnbauer C, Levchuk I, Hou Y, Brabec C J and Forberich K 2016 Coloring semitransparent perovskite solar cells via dielectric mirrors *ACS Nano* **10** 5104–12

[198] Zhang W, Eperon G E and Snaith H J 2016 Metal halide perovskites for energy applications *Nat. Energy* **1** 16048

[199] Eperon G E, Burlakov V M, Goriely A and Snaith H J 2014 Neutral color semitransparent microstructured perovskite solar cells *ACS Nano* **8** 591–8

[200] Hörantner M T, Nayak P K, Mukhopadhyay S, Wojciechowski K, Beck C, McMeekin D, Kamino B, Eperon G E and Snaith H J 2016 Shunt-blocking layers for semitransparent perovskite solar cells *Adv. Mater. Interfaces* **3** 1500837

[201] Pracchia J A and Simon J M 1981 Transparent heat mirrors: influence of the materials on the optical characteristics: addendum *Appl. Opt.* **20** 251–8

[202] Yang Y, Chen Q, Hsieh Y T, Song T B, De Marco N, Zhou H and Yang Y 2015 Multilayer transparent top electrode for solution processed perovskite/Cu(In,Ga)$(Se,S)_2$ four terminal tandem solar cells *ACS Nano* **9** 7714–21

[203] Roldán-Carmona C, Malinkiewicz O, Betancur R, Longo G, Momblona C, Jaramillo F, Camacho L and Bolink H J 2014 High efficiency single-junction semitransparent perovskite solar cells *Energy Environ. Sci.* **7** 2968–73

[204] Jung J W, Chueh C C and Jen A K Y 2015 High-performance semitransparent perovskite solar cells with 10% power conversion efficiency and 25% average visible transmittance based on transparent CuSCN as the hole-transporting material *Adv. Energy Mater.* **5** 1500486

[205] Li Z *et al* 2014 Laminated carbon nanotube networks for metal electrode-free efficient perovskite solar cells *ACS Nano* **8** 6797–804

[206] You P, Liu Z, Tai Q, Liu S and Yan F 2015 Efficient semitransparent perovskite solar cells with graphene electrodes *Adv. Mater.* **27** 3632–8

[207] Yang K, Li F, Zhang J, Veeramalai C P and Guo T 2016 All-solution processed semi-transparent perovskite solar cells with silver nanowires electrode *Nanotechnology* **27** 95202

[208] Guo F, Azimi H, Hou Y, Przybilla T, Hu M, Bronnbauer C, Langner S, Spiecker E, Forberich K and Brabec C J 2014 High-performance semitransparent perovskite solar cells with solution-processed silver nanowires as top electrodes *Nanoscale* **7** 1642–9

[209] Bryant D, Greenwood P, Troughton J, Wijdekop M, Carnie M, Davies M, Wojciechowski K, Snaith H J, Watson T and Worsley D 2014 A transparent conductive adhesive laminate electrode for high-efficiency organic–inorganic lead halide perovskite solar cells *Adv. Mater.* **26** 7499–504

[210] Heo J H, Han H J, Lee M, Song M, Kim D H and Im S H 2015 Stable semi-transparent $CH_3NH_3PbI_3$ planar sandwich solar cells *Energy Environ. Sci.* **8** 2922–7

[211] Bush K A, Bailie C D, Chen Y, Bowring A R, Wang W, Ma W, Leijtens T, Moghadam F and McGehee M D 2016 Thermal and environmental stability of semi-transparent perovskite solar cells for tandems enabled by a solution-processed nanoparticle buffer layer and sputtered ITO electrode *Adv. Mater.* **28** 3937–43

[212] Fu F, Feurer T, Jäger T, Avancini E, Bissig B, Yoon S, Buecheler S and Tiwari A N 2015 Low-temperature-processed efficient semi-transparent planar perovskite solar cells for bifacial and tandem applications *Nat. Commun.* **6** 8932

[213] Acik M and Darling S B 2016 Graphene in perovskite solar cells: device design, characterization and implementation *J. Mater. Chem.* A **4** 6185–235

[214] Bae S *et al* 2010 Roll-to-roll production of 30 inch graphene films for transparent electrodes *Nat. Nanotechnol.* **5** 574–8

[215] Ramírez Quiroz C O, Levchuk I, Bronnbauer C, Salvador M, Forberich K, Heumüller T, Hou Y, Schweizer P, Spiecker E and Brabec C J 2015 Pushing efficiency limits for semitransparent perovskite solar cells *J. Mater. Chem.* A **3** 24071–81

[216] Hsu H L, Chang C C, Chen C P, Jiang B H, Jeng R J and Cheng C H 2015 High-performance and high-durability perovskite photovoltaic devices prepared using ethylammonium iodide as an additive *J. Mater. Chem.* A **3** 9271–7

[217] Tiep N H, Ku Z and Fan H J 2016 Recent advances in improving the stability of perovskite solar cells *Adv. Energy Mater.* **6** 1501420

[218] Yi C, Luo J, Meloni S, Boziki A, Ashari-Astani N, Grätzel C, Zakeeruddin S M, Röthlisberger U and Grätzel M 2016 Entropic stabilization of mixed A-cation ABX_3 metal halide perovskites for high performance perovskite solar cells *Energy Environ. Sci.* **9** 656–62

[219] Weerasinghe H C, Dkhissi Y, Scully A D, Caruso R A and Cheng Y B 2015 Encapsulation for improving the lifetime of flexible perovskite solar cells *Nano Energy* **18** 118–25

[220] Lee S J, Shin S S, Kim Y C, Kim D, Ahn T K, Noh J H, Seo J and Seok S Il 2016 Fabrication of efficient formamidinium tin iodide perovskite solar cells through SnF_2-pyrazine complex *J. Am. Chem. Soc.* **138** 3974–7

[221] Gardner K L *et al* 2016 Nonhazardous solvent systems for processing perovskite photovoltaics *Adv. Energy Mater.* **6** 1600386

[222] Nunzi J M 2002 Organic photovoltaic materials and devices *C. R. Phys.* **3** 523–42

[223] Krebs F C, Espinosa N, Hösel M, Søndergaard R R and Jørgensen M 2014 25th anniversary article: rise to power-OPV-based solar parks *Adv. Mater.* **26** 29–39

[224] Scharber M C and Sariciftci N S 2013 Efficiency of bulk-heterojunction organic solar cells *Prog. Polym. Sci.* **38** 1929–40

[225] Liu Y, Zhao J, Li Z, Mu C, Ma W, Hu H, Jiang K, Lin H, Ade H and Yan H 2014 Aggregation and morphology control enables multiple cases of high-efficiency polymer solar cells *Nat. Commun.* **5** 5293

[226] Zhu F 2014 Semitransparent organic solar cells *Front. Optoelectron.* **7** 20–7

[227] Yip H and Jen A K Y 2016 Semi-transparent polymer solar cells for power generating window applications *Polymer Photovoltaics: Materials, Physics, and Device Engineering* (Cambridge: Royal Society of Chemistry) pp 352–75

[228] Kang H, Kim G, Kim J, Kwon S, Kim H and Lee K 2016 Bulk-heterojunction organic solar cells: five core technologies for their commercialization *Adv. Mater.* **28** 7821–61

[229] Ameri T, Dennler G, Waldauf C, Azimi H, Seemann A, Forberich K, Hauch J, Scharber M, Hingerl K and Brabec C J 2010 Fabrication, optical modeling, and color characterization of semitransparent bulk-heterojunction organic solar cells in an inverted structure *Adv. Funct. Mater.* **20** 1592–8

[230] Chen K S, Salinas J F, Yip H L, Huo L, Hou J and Jen A K Y 2012 Semi-transparent polymer solar cells with 6% PCE, 25% average visible transmittance and a color rendering index close to 100 for power generating window applications *Energy Environ. Sci.* **5** 9551–7
[231] Chueh C C, Chien S C, Yip H L, Salinas J F, Li C Z, Chen K S, Chen F C, Chen W C and Jen A K Y 2013 Toward high-performance semi-transparent polymer solar cells: optimization of ultra-thin light absorbing layer and transparent cathode architecture *Adv. Energy Mater.* **3** 417–23
[232] Chang C Y, Zuo L, Yip H L, Li Y, Li C Z, Hsu C S, Cheng Y J, Chen H and Jen A K Y 2013 A versatile fluoro-containing low-bandgap polymer for efficient semitransparent and tandem polymer solar cells *Adv. Funct. Mater.* **23** 5084–90
[233] Dou L, Gao J, Richard E, You J, Chen C C, Cha K C, He Y, Li G and Yang Y 2012 Systematic investigation of benzodithiophene- and diketopyrrolopyrrole- based low-bandgap polymers designed for single junction and tandem polymer solar cells *J. Am. Chem. Soc.* **134** 10071–9
[234] Dou L, Chang W H, Gao J, Chen C C, You J and Yang Y 2013 A selenium-substituted low-bandgap polymer with versatile photovoltaic applications *Adv. Mater.* **25** 825–31
[235] Zhou J *et al* 2013 Solution-processed and high-performance organic solar cells using small molecules with a benzodithiophene unit *J. Am. Chem. Soc.* **135** 8484–7
[236] Meiss J, Holzmueller F, Gresser R, Leo K and Riede M 2011 Near-infrared absorbing semitransparent organic solar cells *Appl. Phys. Lett.* **99** 193307
[237] Lunt R R and Bulovic V 2011 Transparent, near-infrared organic photovoltaic solar cells for window and energy-scavenging applications *Appl. Phys. Lett.* **98** 113305
[238] Meiss J, Leo K, Riede M K, Uhrich C, Gnehr W M, Sonntag S and Pfeiffer M 2009 Efficient semitransparent small-molecule organic solar cells *Appl. Phys. Lett.* **95** 213306
[239] Bailey-Salzman R F, Rand B P and Forrest S R 2006 Semitransparent organic photovoltaic cells *Appl. Phys. Lett.* **88** 233502
[240] Min J *et al* 2016 Fully solution-processed small molecule semitransparent solar cells: optimization of transparent cathode architecture and four absorbing layers *Adv. Funct. Mater.* **26** 4543–50
[241] Ren X, Li X and Choy W C H 2015 Optically enhanced semi-transparent organic solar cells through hybrid metal/nanoparticle/dielectric nanostructure *Nano Energy* **17** 187–95
[242] Tao C, Xie G, Liu C, Zhang X, Dong W, Meng F, Kong X, Shen L, Ruan S and Chen W 2009 Semitransparent inverted polymer solar cells with MoO_3/Ag/MoO_3 as transparent electrode *Appl. Phys. Lett.* **95** 53303
[243] Donggeon H, Hoyeon K, Soohyun L, Myungsoo S and and Seunghyup Y 2010 Realization of efficient semitransparent organic photovoltaic cells with metallic top electrodes: utilizing the tunable absorption asymmetry *Opt. Express* **18** A513–21
[244] Li F, Ruan S, Xu Y, Meng F, Wang J, Chen W and Shen L 2011 Semitransparent inverted polymer solar cells using MoO_3/Ag/WO_3 as highly transparent anodes *Sol. Energy Mater. Sol. Cells* **95** 877–80
[245] Shen L, Ruan S, Guo W, Meng F and Chen W 2011 Semitransparent inverted polymer solar cells using MoO_3/Ag/V_2O_5 as transparent anodes *Org. Electron.* **12** 1223–6
[246] Winkler T *et al* 2011 Efficient large area semitransparent organic solar cells based on highly transparent and conductive ZTO/Ag/ZTO multilayer top electrodes *Org. Electron. Phys. Mater. Appl.* **12** 1612–8
[247] Guo F *et al* 2013 ITO-free and fully solution-processed semitransparent organic solar cells with high fill factors *Adv. Energy Mater.* **3** 1062–7
[248] Zhou Y, Li F, Barrau S, Tian W, Inganäs O and Zhang F 2009 Inverted and transparent polymer solar cells prepared with vacuum-free processing *Sol. Energy Mater. Sol. Cells* **93** 497–500
[249] Kang J W, Kang Y J, Jung S, You D S, Song M, Kim C S, Kim D G, Kim J K and Kim S H 2012 All-spray-coated semitransparent inverted organic solar cells: from electron selective to anode layers *Org. Electron. Phys. Mater. Appl.* **13** 2940–4
[250] Larsen-Olsen T T, Søndergaard R R, Norrman K, Jørgensen M and Krebs F C 2012 All printed transparent electrodes through an electrical switching mechanism: a convincing alternative to indium-tin-oxide, silver and vacuum *Energy Environ. Sci.* **5** 9467–71
[251] Chaudhary S, Lu H, Müller A M, Bardeen C J and Ozkan M 2007 Hierarchical placement and associated optoelectronic impact of carbon nanotubes in polymer-fullerene solar cells *Nano Lett.* **7** 1973–9
[252] Nickel F, Puetz A, Reinhard M, Do H, Kayser C, Colsmann A and Lemmer U 2010 Cathodes comprising highly conductive poly(3,4-ethylenedioxythiophene): poly(styrenesulfonate) for semi-transparent polymer solar cells *Org. Electron.* **11** 535–8
[253] Dong Q, Zhou Y, Pei J, Liu Z, Li Y, Yao S, Zhang J and Tian W 2010 All-spin-coating vacuum-free processed semi-transparent inverted polymer solar cells with PEDOT: PSS anode and PAH-D interfacial layer *Org. Electron.* **11** 1327–31
[254] Huang J, Li G and Yang Y 2008 A semi-transparent plastic solar cell fabricated by a lamination process *Adv. Mater.* **20** 415–9
[255] Spyropoulos G D *et al* 2016 A universal solution-processing method for organic and perovskite solar modules innovated by adhesive top electrode *Energy Environ. Sci.* **9** 2302–13
[256] Zhang H, Wicht G, Gretener C, Nagel M, Nüesch F, Romanyuk Y, Tisserant J-N and Hany R 2013 Semitransparent organic photovoltaics using a near-infrared absorbing cyanine dye *Sol. Energy Mater. Sol. Cells* **118** 157–64
[257] Vandewal K, Tvingstedt K, Gadisa A, Inganäs O and Manca J V 2009 On the origin of the open-circuit voltage of polymer–fullerene solar cells *Nat. Mater.* **8** 904–9
[258] Lunt R R 2012 Theoretical limits for visibly transparent photovoltaics *Appl. Phys. Lett.* **101** 043902
[259] Sha W E I, Ren X, Chen L and Choy W C H 2015 The efficiency limit of $CH_3NH_3PbI_3$ perovskite solar cells *Appl. Phys. Lett.* **106** 221104
[260] Xue H, Wu R, Xie Y, Tan Q, Qin D, Wu H and Huang W 2016 Recent progress on solution-processed CdTe nanocrystals solar cells *Appl. Sci.* **6** 197
[261] Niu G, Guo X and Wang L 2015 Review of recent progress in chemical stability of perovskite solar cells *J. Mater. Chem.* A **3** 8970–80
[262] Hagberg D P *et al* 2008 Molecular engineering of organic sensitizers for dye-sensitized solar cell applications *J. Am. Chem. Soc.* **130** 6259–66
[263] Yoo S H 2011 Simulation for an optimal application of BIPV through parameter variation *Sol. Energy* **85** 1291–301
[264] Liu Y, Shen H, Huang X and Deng Y 2006 A new improved structure of dye-sensitized solar cells with reflection film *Chin. Sci. Bull.* **51** 369–73
[265] Li H, Zhao Q, Wang W, Dong H, Xu D, Zou G, Duan H and Yu D 2013 Novel planar-structure electrochemical devices for highly flexible semitransparent power generation/storage sources *Nano Lett.* **13** 1271–7

[266] Premaratne K, Kumara G R A, Rajapakse R M G and Karunarathne M L 2012 Highly efficient, optically semi-transparent, ZnO-based dye-sensitized solar cells with indoline D-358 as the dye *J. Photochem. Photobiol.* A **229** 29–32

[267] Chang C Y, Lee K T, Huang W K, Siao H Y and Chang Y C 2015 High-performance, air-stable, low-temperature processed semitransparent perovskite solar cells enabled by atomic layer deposition *Chem. Mater.* **27** 5122–30

[268] Yim J H, Joe S Y, Pang C, Lee K M, Jeong H, Park J Y, Ahn Y H, De Mello J C and Lee S 2014 Fully solution-processed semitransparent organic solar cells with a silver nanowire cathode and a conducting polymer anode *ACS Nano* **8** 2857–63

[269] Guo F, Kubis P, Stubhan T, Li N, Baran D, Przybilla T, Spiecker E, Forberich K and Brabec C J 2014 Fully solution-processing route toward highly transparent polymer solar cells *ACS Appl. Mater. Interfaces* **6** 18251–7

[270] Lee J Y, Connor S T, Cui Y and Peumans P 2010 Semitransparent organic photovoltaic cells with laminated top electrode *Nano Lett.* **10** 1276–9

[271] Bauer A, Wahl T, Hanisch J and Ahlswede E 2012 ZnO:Al cathode for highly efficient, semitransparent 4 organic solar cells utilizing TiO_x and aluminum interlayers *Appl. Phys. Lett.* **100** 073307